

Soft Multicopter Control using Neural Dynamics Identification

Yitong Deng^{1*}, Yaorui Zhang¹, Xingzhe He¹, Shuqi Yang¹, Yunjin Tong¹
Michael Zhang², Daniel DiPietro¹, Bo Zhu¹

¹Computer Science Department, Dartmouth College

²Lawrenceville School

* yitong.deng.gr@dartmouth.edu

Abstract: Dynamic control of a soft-body robot to deliver complex behaviors with low-dimensional actuation inputs is challenging. In this paper, we present a computational approach to automatically generate underactuated control policies for soft multicopters, featured by their elastic material components, non-conventional shapes, and asymmetric rotor layouts, to precisely deliver compliant deformation and agile locomotion. The central piece of our approach lies in a lightweight, physics-inspired neural network model to identify the dynamics of a set of geometric variables characterizing an elastic soft body. In particular, we decompose the rotation, translation, and pure deformation components of a soft multicopter and train a learning model to predict their nonlinear couplings. This model is further integrated into a Linear Quadratic Regulator (LQR) control loop equipped with a set of standard Inertial Measurement Units (IMUs). We designed a novel online relinearization scheme to enable the LQR control of soft-body balancing, allowing an aggressive reduction of the computational overhead caused by the conventional full-scale sensing-simulation-control workflow. We demonstrate the efficacy of our approach by generating controllers for a broad spectrum of customized soft multicopter designs and testing them in a high-fidelity physics simulation environment. Our algorithm enables the multicopters to perform a variety of tasks, including hovering, tracking, cruising and active deforming.

Keywords: Soft multicopter, compliant mechanics, learning-based control, LQR controller, physics-based neural networks

1 Introduction

Making a drone body soft opens up brand new horizons to improve its safety, maneuverability, and functionalities. The intrinsic property of soft materials to deform and absorb energy during collision allows safe human-machine interactions [1, 2, 3]. Drones that can deform itself are naturally better than rigid ones for its capability of actively deforming to change its size and shape to travel through difficult, confined terrains. Also, the ability of soft drones to deform in a controlled manner while maintaining its position and orientation essentially enables them to perform secondary functionalities, apart from merely flying in the air. For instance, a soft drone can fold inward, fold outward, and switch between these two states per user specification, opening up possibilities in enabling novel functionalities such as grasping, gliding, and flapping, without requiring any additional mechanical assemblies or designs.

The rigid-body drone family achieved tremendous success over the last decade, however, the development of drones made of soft materials remains in its infancy due to the multi-faceted challenges intrigued by the partially sensed data, expensive deformation modeling, underactuated rotor control, and their system-level integrations. Among these challenges, the difficulty of obtaining proprioceptive data from sparse samples, and the highly underactuated control of an infinite collection of material points with a finite set of rotor inputs, are jointly acting as the main obstacles that prevents the direct transfer of the various mature techniques invented for rigid drones. In particular, in the rigid-body drone realm, Inertial Measurement Unit (IMU) + Linear Quadratic Regulator (LQR) is a

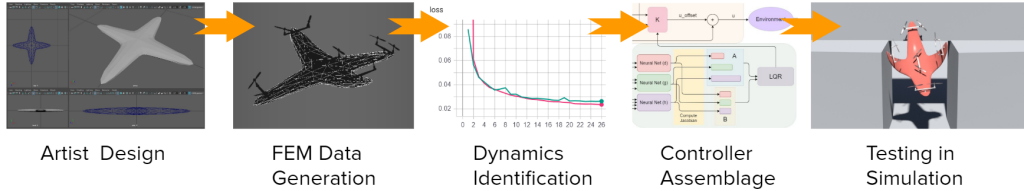


Figure 1: System overview: the workflow of our system consists of five stages to automate the control policy generation procedure for a soft drone design.

classical combination to establish a control loop that can effectively maneuver the body locomotion within a 6-dimensional phase space. However, neither of these techniques can be applied directly to control soft drones. One particular reason is that the deformation of a soft body cannot be reconstructed from a small set of orientation (IMU) data. Various types of new sensors (e.g., bending [4], thermal [5], fluidic [6]) or new data-driven models (e.g., differentiable simulators) have been invented to tackle the challenge, which, at the same time, raised the system complexity and the computational cost significantly when compared with its rigid counterpart.

This paper aims to tackle these two challenges by establishing a novel control approach empowered by a neural dynamics identification algorithm. Our control algorithm takes the IMU sensing data as input and builds the control-loop based on LQR, which inherently connects to the various mature hardware and software built for rigid drones. Our key insight is that we can characterize a soft body’s deformation with simple neural networks by incorporating inductive priors that reveals the underpinning kinematics of a deformed body. In particular, we decompose a local body frame into its rotation, translation, and pure deformation components. These geometric components, along with their nonlinear interactions, can be modelled using a learning-based approach and incorporated in an enhanced LQR controller to generate effective control policies. The proposed technique naturally bridges the soft and rigid drone communities by demonstrating benefits regarding both system design and computational efficiency.

As shown in Figure 1, our system takes soft drone geometries with customized rotor and sensor configurations as input, and returns a functional that computes full-state feedback control matrices depending on the drone’s current state. Our approach can not only manage the soft drones to hover, reach a particular position, maintain a particular attitude and/or velocity, which are challenging tasks on their own, but also control them to actively deform into shapes as specified. To the best of our knowledge, the proposed approach is the first computational system that obtains controllers for substantially soft multicopters (those that will fail badly when controlled with a rigid controller).

2 Related Work

Multicopter Control In recent years, multicopters have emerged to dominance in the realm of commercial UAVs, thanks to their simple mechanical structures, optimized efficiency for hovering, and easy-to-control dynamics [7, 8]. Quadcopter, with its simplistic and symmetrical design, is undoubtedly the most popular one, with its dynamics and control well-studied by [9, 10, 11] and etc. Various methods have been successfully developed to control multicopters, including PD/PID [9], LQR [12, 13], differential flatness [10], integral sliding mode [14], and MPC [15] methods. Nonconventional geometries [12], hybrid wing-copter modes [16], articulated structures [17, 18], and foldable structures [19] have been tackled in the controller design problem. Recent works also been done to extend drone’s ability to actively deform itself to pass through tight spaces [17, 20] or to perform secondary functionalities like grasping [21], via elaborately designed assembly of linked multicopters.

Learning-based Soft-Body Control The control of soft robots has been extensively studied [22]. However, up to date it remains a very challenging topic due to the underactuated nature of the high-dimensional phase space for a soft body [1]. A broad array of control mechanics, including the simulation-driven control [23], morphological computing schemes [24], and learning-based physics

simulators [25, 26] have been proposed to reduce the complexity or accelerate the computation of a soft-body control problem.

3 Dynamics Identification

3.1 Soft Multicopter Dynamics

We consider a soft body Ω connected with n rotors. Let \mathbf{X} be the material coordinates of points in a body domain Ω and \mathbf{x} be their world-space coordinates. The two coordinate systems are bridged by a deformation mapping $\mathbf{x} = \Phi(\mathbf{X})$. The soft material model is described by its density ρ , damping γ , and an elasticity model denoted by a functional $\epsilon(\Phi)$. In the simulation code, ϵ can be implemented as a Neo-Hookean model, co-rotated model, and so on [27, 28]. Note that our control mechanism is independent from any deformable model implementation, meaning that it can work with different numerical or real-world deformable systems by observing different data sets. A rotor on a soft drone is defined by a tuple $\{u_i, \lambda_i, \mathbf{T}_i, \mathbf{r}_i\}$, with u_i as the magnitude of the propeller thrust, λ_i as the spinning direction, \mathbf{T}_i as the thrust direction in the world space, and \mathbf{r}_i as the rotor position in the material space. We assume each rotor is stick to a local point near the surface of the body in material space. The rotor direction is given as the average of the surface normals in the local region around \mathbf{r}_i , i.e., $\mathbf{T}_i = \sum_{j \in Nb(i)} \mathbf{n}_j / |\sum_{j \in Nb(i)} \mathbf{n}_j|$ in a discrete setting, with \mathbf{n}_j as the normal direction of a neighboring surface triangle.

From Newton’s second law, the soft multicopter dynamics can be written as:

$$\ddot{\mathbf{x}} + \gamma \dot{\mathbf{x}} + \nabla_{\mathbf{x}} \epsilon = \mathbf{b}(\mathbf{X}) + \mathbf{g}. \quad (1)$$

The left-hand side of Equation 1 describes the soft body’s internal forces, including the inertial force, damping force, and elastic force. The right-hand side describes the body’s external forces, including the thrust input $\mathbf{b}(\mathbf{r}_i) = \lambda_i u_i \mathbf{T}_i$, and the gravity \mathbf{g} . Compared with the rigid-body multicopter dynamics equation (e.g., see [12]), the soft-body version does not have the Euler’s equation to describe the body’s rotational movement. The torque effect of a rotor is considered in the elastic solve by enforcing boundary conditions from \mathbf{b} . The spinning torque effect is eliminated on the design stage by implementing each rotor as a pair of propellers spinning in the opposite directions.

3.2 Geometric Representation

The design philosophy of our geometric representation is motivated by the rigid-deformable coordinate decomposition technique proposed in [29] and applied in many following reduced deformable simulators [30, 31, 32]. The key insight is to view a soft body’s deformation as a decomposition of three components: rotation, translation, and pure deformation. Mathematically, for a point \mathbf{X}_i in material space, the relationship among the three components can be written as:

$$\Phi(\mathbf{X}_i) = \mathbf{R}(\mathbf{e})\mathbf{S}(\mathbf{X}_i) + \mathbf{T}(\mathbf{p}), \quad (2)$$

with $\mathbf{p}, \mathbf{e} \in \mathbf{R}^3$ describing the position and orientation of a local rigid frame bind to the soft body, $\mathbf{R}, \mathbf{T} \in \mathbf{R}^{3 \times 3}$ as the corresponding rotation and translation matrices, and $\mathbf{S}(\mathbf{X}_i)$ describes the pure deformation mapping of \mathbf{X}_i within the local frame.

For a rigid drone, the state of the drone at any given time can be uniquely determined by \mathbf{p} , \mathbf{e} , and their derivatives, i.e., $\mathbf{x}^T := [\mathbf{p}, \dot{\mathbf{p}}, \mathbf{e}, \dot{\mathbf{e}}]$, by assuming $\mathbf{S}(\mathbf{X}_i) = \mathbf{X}_i$. However, for deformable drones, due to the existence of non-constant \mathbf{S} , the combination of \mathbf{p} and \mathbf{e} no longer determines the drone’s configuration uniquely, in particular, since particles in deformable bodies can move independently, a single rotation matrix cannot describe the distribution of particles, thereby leaving ambiguities for information such as rotor positions, orientations, moment of inertia which all influence the drone’s dynamics significantly. As a result, we seek to extend the state space to eliminate these ambiguities. Inspired by Equation 2, we extend the previous state with an additional vector $\mathbf{s} \in \mathbf{R}^m$ (m can be arbitrary) that represents the deformation in body frame which \mathbf{e} defines. So now we have $\mathbf{x}^T := [\mathbf{s}, \dot{\mathbf{s}}, \mathbf{e}, \dot{\mathbf{e}}, \mathbf{p}, \dot{\mathbf{p}}]$ (see Figure 2 for an example).

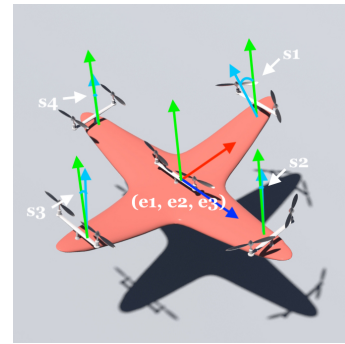


Figure 2: Geometric representation of a soft multicopter

The next step is to formulate the temporal evolution equations given a new set of \mathbf{x} with decomposed components. Here we use three new functions $\{\mathbf{d}, \mathbf{g}, \mathbf{h}\}$ to describe the temporal relations among $\{\mathbf{s}, \mathbf{e}, \mathbf{p}\}$ and the rotor thrusts $\{\mathbf{u}\}$. We make a reasonable assumption that the dynamics of pure deformation will not be influenced by rotation or translation, *i.e.*, $\dot{\mathbf{s}}_{next} = \mathbf{d}(\mathbf{s}, \dot{\mathbf{s}}, \mathbf{u})$ for some function \mathbf{d} ; the dynamics of rotation will not be influenced by position, *i.e.*, $\dot{\mathbf{e}}_{next} = \mathbf{g}(\mathbf{s}, \dot{\mathbf{s}}, \mathbf{e}, \dot{\mathbf{e}}, \mathbf{u})$ for some function \mathbf{g} ; the dynamics of the position will be influenced by deformation, rotation as well as velocity *i.e.*, $\dot{\mathbf{p}}_{next} = \mathbf{h}(\mathbf{s}, \dot{\mathbf{s}}, \mathbf{e}, \dot{\mathbf{e}}, \dot{\mathbf{p}}, \mathbf{u})$ for some function \mathbf{h} . Therefore, in state-space form, the dynamics will be expressed as follows:

$$\dot{\mathbf{x}} = \mathbf{f}(\mathbf{x}, \mathbf{u}) = \begin{bmatrix} \dot{\mathbf{s}} \\ \dot{\mathbf{s}} \\ \dot{\mathbf{e}} \\ \dot{\mathbf{e}} \\ \dot{\mathbf{p}} \\ \dot{\mathbf{p}} \end{bmatrix} = \begin{bmatrix} \dot{\mathbf{s}} \\ \frac{1}{\alpha}(\mathbf{d}(\mathbf{s}, \dot{\mathbf{s}}, \mathbf{u}) - \dot{\mathbf{s}}) \\ \dot{\mathbf{e}} \\ \frac{1}{\alpha}(\mathbf{g}(\mathbf{s}, \dot{\mathbf{s}}, \mathbf{e}, \dot{\mathbf{e}}, \mathbf{u}) - \dot{\mathbf{e}}) \\ \dot{\mathbf{p}} \\ \frac{1}{\alpha}(\mathbf{h}(\mathbf{s}, \dot{\mathbf{s}}, \mathbf{e}, \dot{\mathbf{e}}, \dot{\mathbf{p}}, \mathbf{u}) - \dot{\mathbf{p}}) \end{bmatrix}, \quad (3)$$

where α represents the timelapse between sensor updates, \mathbf{s} represents the the set of Earth-frame orientation readings from selected regions, viewed in the drone's local frame, which is defined by the measurement of \mathbf{e} , and then converted into a single angle with the y vector in the local frame.

3.3 Learning-based identification

We train three simple neural networks to learn $\{\mathbf{d}, \mathbf{g}, \mathbf{h}\}$, respectively. We use the residual block [33] with convolution layers replaced by linear layers, as previously explored by [34, 35]. We do not use any normalization throughout the networks. The neural networks consist of four residual blocks followed by one linear layer. All three functions share the same network architecture but different parameter weights. We refer the readers to the supplementary for the training details.

4 Dynamics Control

After the learning is complete, the dynamic model that $\{\mathbf{d}, \mathbf{g}, \mathbf{h}\}$ together constitutes will be optimized by the LQR to yield the control policy (see Figure 3 for an overview). As LQR requires a linear system, we will perform first-order Taylor expansion around an operating point, which involves extracting the networks' Jacobian matrices with respect to that point, a process carried out with automatic differentiation. Once the linearized system is obtained, the LQR will provide a control matrix \mathbf{K} , which serves directly as our feedback policy with $\mathbf{u} = -\mathbf{K}\mathbf{x}$. Meanwhile, the selection of the operating point is crucial. Conventionally, a fixed point $(\mathbf{x}^*, \mathbf{u}^*)$ such that $\mathbf{f}(\mathbf{x}^*, \mathbf{u}^*) = \mathbf{0}$ is used. However, as such fixed points are difficult to obtain for soft materials, we propose an online relinearization algorithm that can operate without the explicit knowledge of a fixed point. The relinearization will be carried out at 10Hz, whereas the control policy will be applied at 100Hz. The control strategy will be further described in the following sections.

4.1 LQR for Soft Body Control

Given a linear system $\dot{\mathbf{x}} = \mathbf{A}\mathbf{x} + \mathbf{B}\mathbf{u}$, LQR generates the optimal control policy $\mathbf{u} = -\mathbf{K}\mathbf{x}$ that drives \mathbf{x} to zero with the minimal actuation \mathbf{u} by minimizing the cost function $\int_0^\infty (\mathbf{x}^T \mathbf{Q} \mathbf{x} + \mathbf{u}^T \mathbf{R} \mathbf{u}) dt$. The \mathbf{Q} and \mathbf{R} matrices are cost matrices used to manage the tradeoff between fast effect and fuel economy. The optimization is carried out via solving the Continuous-time Algebraic Riccati Equation, which we will carry out with SciPy. To apply the LQR to a non-linear system, we linearize the system's dynamics given in Equation 3 by conducting a first-order Taylor expansion around some operating point $(\mathbf{x}^*, \mathbf{u}^*)$. The linearized system is like:

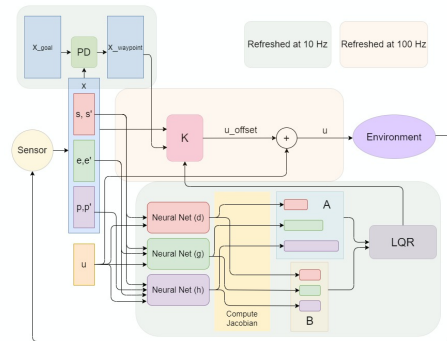


Figure 3: Neural LQR controller architecture

$$\dot{\mathbf{x}} = \mathbf{f}(\mathbf{x}, \mathbf{u}) \approx \mathbf{f}(\mathbf{x}^*, \mathbf{u}^*) + \mathbf{A}(\mathbf{x} - \mathbf{x}^*) + \mathbf{B}(\mathbf{u} - \mathbf{u}^*), \quad (4)$$

where $\mathbf{A} = \frac{\partial \mathbf{f}}{\partial \mathbf{x}}|_{\mathbf{x}^*, \mathbf{u}^*}$, and $\mathbf{B} = \frac{\partial \mathbf{f}}{\partial \mathbf{u}}|_{\mathbf{x}^*, \mathbf{u}^*}$, details shown in Equation 5.

$$\mathbf{A} = \begin{bmatrix} \mathbf{O} & \mathbf{I} & \mathbf{O} & \mathbf{O} & \mathbf{O} & \mathbf{O} \\ \frac{1}{\alpha} \frac{\partial \mathbf{d}}{\partial \mathbf{s}} & \frac{1}{\alpha} (\frac{\partial \mathbf{d}}{\partial \mathbf{s}} - \mathbf{I}) & \mathbf{O} & \mathbf{O} & \mathbf{O} & \mathbf{O} \\ \mathbf{O} & \mathbf{O} & \mathbf{O} & \mathbf{I} & \mathbf{O} & \mathbf{O} \\ \frac{1}{\alpha} \frac{\partial \mathbf{g}}{\partial \mathbf{s}} & \frac{1}{\alpha} \frac{\partial \mathbf{g}}{\partial \mathbf{s}} & \frac{1}{\alpha} \frac{\partial \mathbf{g}}{\partial \mathbf{e}} & \frac{1}{\alpha} (\frac{\partial \mathbf{g}}{\partial \mathbf{e}} - \mathbf{I}) & \mathbf{O} & \mathbf{O} \\ \mathbf{O} & \mathbf{O} & \mathbf{O} & \mathbf{O} & \mathbf{O} & \mathbf{I} \\ \frac{1}{\alpha} \frac{\partial \mathbf{h}}{\partial \mathbf{s}} & \frac{1}{\alpha} \frac{\partial \mathbf{h}}{\partial \mathbf{s}} & \frac{1}{\alpha} \frac{\partial \mathbf{h}}{\partial \mathbf{e}} & \frac{1}{\alpha} \frac{\partial \mathbf{h}}{\partial \mathbf{e}} & \mathbf{O} & \frac{1}{\alpha} (\frac{\partial \mathbf{h}}{\partial \mathbf{p}} - \mathbf{I}) \end{bmatrix}_{\mathbf{x}^*, \mathbf{u}^*} \quad \mathbf{B} = \begin{bmatrix} \mathbf{O} \\ \frac{1}{\alpha} \frac{\partial \mathbf{d}}{\partial \mathbf{u}} \\ \mathbf{O} \\ \frac{1}{\alpha} \frac{\partial \mathbf{g}}{\partial \mathbf{u}} \\ \mathbf{O} \\ \frac{1}{\alpha} \frac{\partial \mathbf{h}}{\partial \mathbf{u}} \end{bmatrix}_{\mathbf{x}^*, \mathbf{u}^*} \quad (5)$$

If we make a further assumption that for $(\mathbf{x}^*, \mathbf{u}^*)$ and (\mathbf{x}, \mathbf{u}) close enough to each other, $\mathbf{f}(\mathbf{x}, \mathbf{u}) - \mathbf{f}(\mathbf{x}^*, \mathbf{u}^*) \approx \mathbf{f}(\mathbf{x} - \mathbf{x}^*, \mathbf{u} - \mathbf{u}^*)$, then we can write the temporal evolution of \mathbf{x} as:

$$(\dot{\mathbf{x}} - \dot{\mathbf{x}}^*) = \mathbf{f}(\mathbf{x} - \mathbf{x}^*, \mathbf{u} - \mathbf{u}^*) \approx \mathbf{A}(\mathbf{x} - \mathbf{x}^*) + \mathbf{B}(\mathbf{u} - \mathbf{u}^*). \quad (6)$$

In that case, applying LQR with \mathbf{A} and \mathbf{B} essentially drives $(\dot{\mathbf{x}} - \dot{\mathbf{x}}^*)$ to $\mathbf{0}$, *i.e.* closing the gap between the current state and the operating state. Conceptually speaking, assuming $\mathbf{f}(\mathbf{x}, \mathbf{u}) - \mathbf{f}(\mathbf{x}^*, \mathbf{u}^*) \approx \mathbf{f}(\mathbf{x} - \mathbf{x}^*, \mathbf{u} - \mathbf{u}^*)$ in our case requires that the difference between the elastic force experienced by two similar deformations is approximately the force experienced by the small deformation representing the difference in their shape, which holds if we assume the dynamics of the abstract deformation approximately is dominated by the Hooke's Law. Similarly, we make the small angle assumption for the rotation dynamics. In practice, we find that this assumption provides satisfactory results when combined with our online relinearization.

4.2 Online Relinearization

Typically, $(\mathbf{x}^*, \mathbf{u}^*)$ are chosen to be fixed points of the dynamics system where $\mathbf{f}(\mathbf{x}^*, \mathbf{u}^*) = \mathbf{0}$. However, for deformable drones, obtaining a fixed point is far from a trivial task. Let us reconsider the control problem. Suppose we want our soft drone to reach a certain configuration *e.g.* a certain position, attitude, velocity or deformed shape, we would typically conjure the target without knowing if it can be a fixed point and what value of \mathbf{u} would fix it there. The system input is simply where we would hope for it to be. But since it is neither a fixed point, or a point close enough to our current point that we cannot apply the proximity assumption in Equation 6, we cannot directly linearize around it.

Algorithm 1 Online Relinearizing LQR

Input: Current state \mathbf{X}_{curr} ;
Goal state \mathbf{X}_{goal} ;
PD gains: kp, kd ;
Number of steps between relinearization n ;
Cost matrices: \mathbf{Q}, \mathbf{R}

- 1: $\mathbf{u}_{curr} \leftarrow \mathbf{0}$
- 2: $iter \leftarrow 0$
- 3: **while** running **do**
- 4: update $\mathbf{X}_{curr}, \dot{\mathbf{X}}_{curr}$
- 5: $iter \leftarrow iter + 1$
- 6: **if** $iter \bmod n = 0$ **then**
- 7: $\mathbf{x}_{wp} \leftarrow kp \times (\mathbf{x}_{goal} - \mathbf{x}_{curr}) + kd \times \dot{\mathbf{x}}_{curr}$
- 8: $\mathbf{A}, \mathbf{B} \leftarrow \mathcal{J}(\mathbf{d}, \mathbf{g}, \mathbf{h}, \mathbf{x}_{curr}, \mathbf{u}_{curr})$
- 9: $\mathbf{K} = LQR(\mathbf{A}, \mathbf{B}, \mathbf{Q}, \mathbf{R})$
- 10: $\mathbf{u}_{oper} \leftarrow \mathbf{u}_{curr}$
- 11: **end if**
- 12: $\mathbf{u}_{curr} \leftarrow -\mathbf{K} \times (\mathbf{x}_{curr} - \mathbf{x}_{wp}) + \mathbf{u}_{oper}$
- 13: **end while**

Our solution is that, since we do not have an operating point to linearize around, we will linearize around the current point – That is not supposed to go wrong. Given such a system, we want to take an incremental step towards the goal with LQR. However, by definition, what the LQR in Equation 13 does is to drive states around it to the current state. Our strategy is that if we want to reach a state \mathbf{X}_{wp} from \mathbf{X}_{curr} , then we will pretend to be at $(\mathbf{X}_{curr} - \mathbf{X}_{wp})$ trying to reach \mathbf{X}_{curr} using the LQR control matrix \mathbf{K} we computed for \mathbf{X}_{curr} . Given the current state \mathbf{X}_{curr} and the goal state \mathbf{X}_{goal} , we calculate \mathbf{X}_{wp} using a PD control scheme, where $\mathbf{X}_{wp} = kp \times (\mathbf{X}_{goal} - \mathbf{X}_{curr}) + kd \times \dot{\mathbf{X}}_{curr}$. The control matrix will be used for n timesteps, before it is updated again to match the new drone status. The full algorithm is described in Algorithm 1.

This algorithm relieves the burden to compute the fixed point $(\mathbf{x}^*, \mathbf{u}^*)$, which makes the user control much simpler. First, instead of inputting a feasible target, the user only needs to specify roughly how it want the target to look like, which is essential for soft drones because most configurations are not feasible.

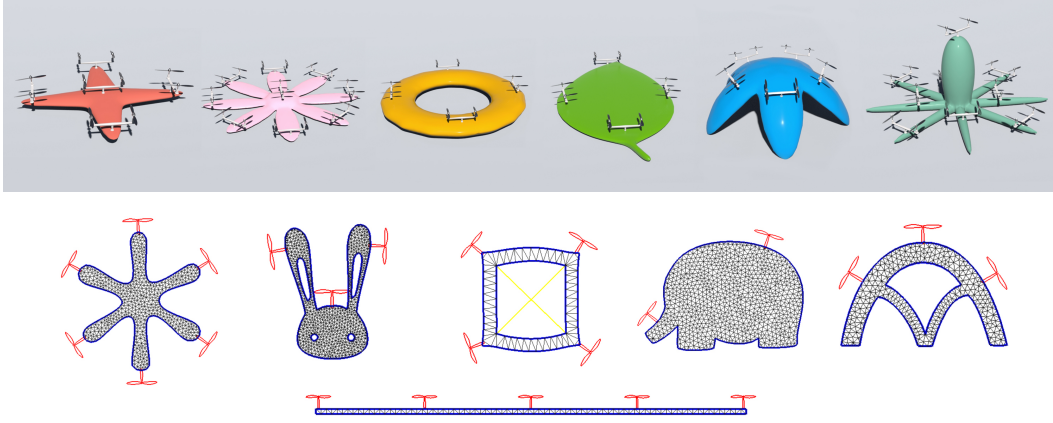


Figure 4: 3D (top) and 2D (bottom) soft drone designs with unconventional shapes and rotor layouts

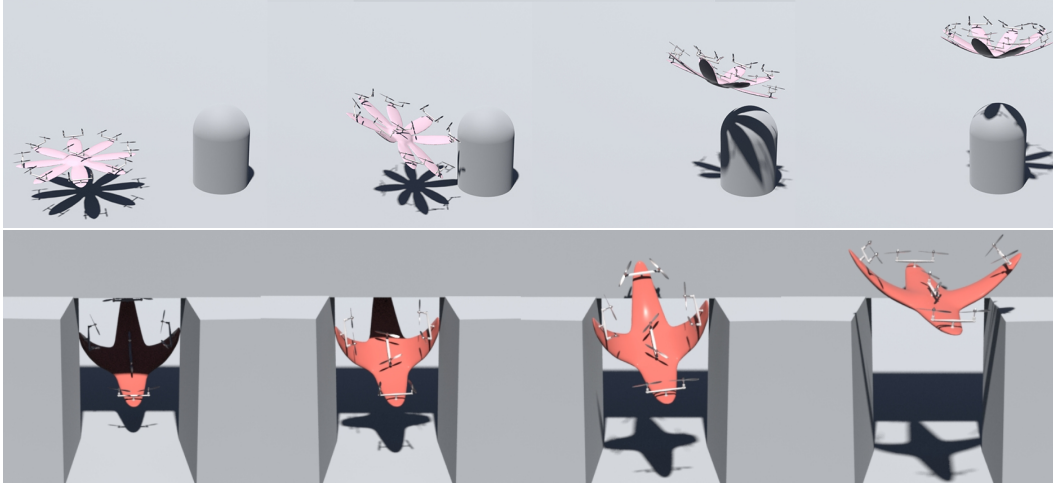


Figure 5: Top: Locomotion animation; Bottom: Obstacle avoidance animation

5 Evaluation and Results

To verify that our system can handle different soft drone designs, we developed a number of different models in both 2D and 3D that include both symmetrical and asymmetrical structures, even and odd number of rotors, single or multiple materials, with virtual springs to add material complexities (see Figure 4). We refer to the supplementary for details about experiment setup and the result videos.

Locomotion Control We demonstrate that for soft drones whose deformation is significant, our method is superior to LQR by far. We implement a traditional LQR controller that is based on the assumption of the rigid nature of each drone’s undeformed shape. The geometry-updating LQR is enhanced with the capacity to observe the deformation of the soft drone at each control step, and update the relevant dynamics information regarding rotor position, orientation and rotational inertia accordingly. The correctness of our benchmark models are verified by changing the modulus to 15 times as much so that it becomes approximately rigid. In the top row of Figure 6, we compare the result of controlling the 3D flower drone in reaching position $(3, 3, 3)$ in space. We see that our method drives each coordinates to the target within 7% error. In comparison, none of the other two controlling methods are able to complete the task or even maintain the drone’s balance in the air. We show that our strategy excels in all three metrics by a huge margin (see the table in the next page).

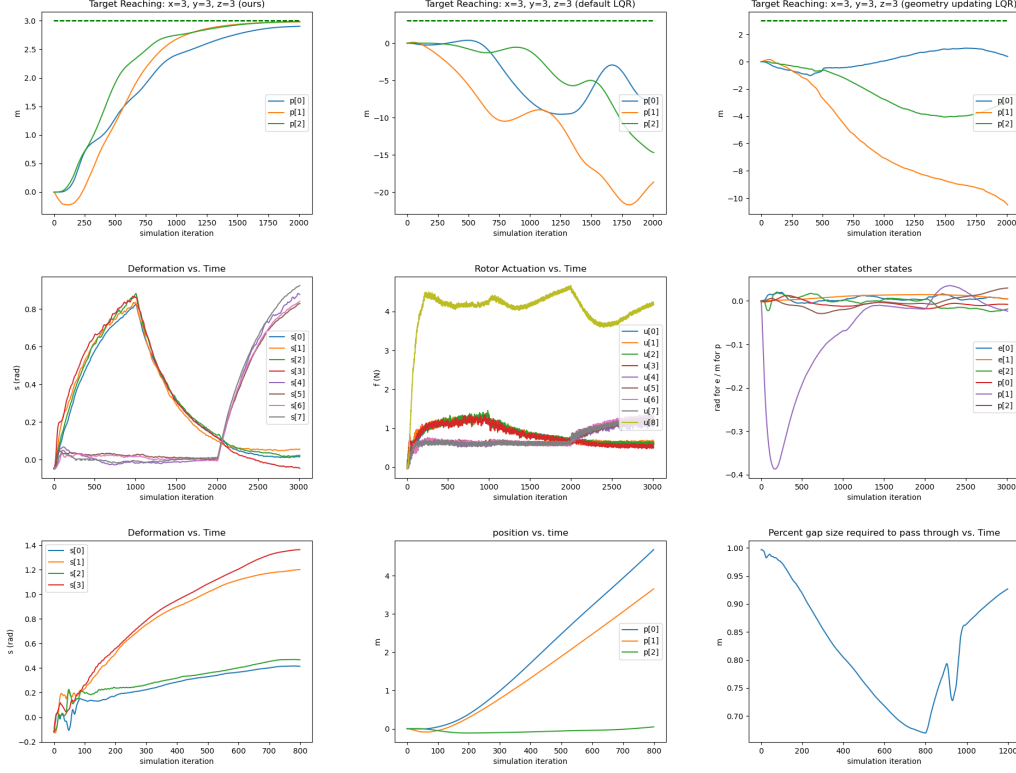


Figure 6: Top: Ours and LQR: Our method (left) drives the drone to the vicinity of our target with high precision. The rigid-LQR derived controllers will fail the task due to the highly varying dynamics of the soft drone; Middle: Deformation Control: Left: deformation level of each sensor. Middle: actuation level of each rotor. Right: stability of rotation and position; Bottom: Obstacle avoid: Left: deformation level of each sensor. Middle: velocity and Euler angles. Right: reduction of length by deformation.

Target Reaching			
metrics	ours	LQR	geometry-updating LQR
survival time (s)	20.0	3.54	5.28
final error (m)	0.126	49.517	22.084
thrust usage (N)	26740	90596	61947

Deformation Control A talent unique to our controller is its ability to decide how the drone is shaped while controlling its locomotion at the same time. In the experiment shown in the middle row of Figure 6, we require the flower drone to maintain at the origin while deforming into two shapes. In the first shape, which is ordered at timestep 0, the lateral pedals lie flat, while the axial pedals rise to produce an angle of 1 radian. In the second shape, which is ordered at timestep 2000, the lateral pedals will rise while the axials will lie flat. As is shown in the second row of Figure 6, each rotors yields extra thrust when the pedal it inhabits is called to lift up. The center rotor takes the main responsibility of maintaining balance and position. As we can see, after the first impact from gravity after the drone is released, the controller is able to precisely fine tune each rotor's thrust so that despite the perturbations in the environment, they are able to keep the Euler angles within $\pm 2^\circ$ and the position within ± 3 centimeters.

From a practical standpoint, the controller's ability to reconcile all three control tasks in altitude, position and deformation at once, enables it to pass through restrained terrains, maintaining a velocity and attitude while deforming in ways to reduce its width or surface area. In the example shown in Figure 5, the drone is challenged with hole between three concrete walls that is narrower than its body. In order to pass through, the human controller will order it to close up the two wings in

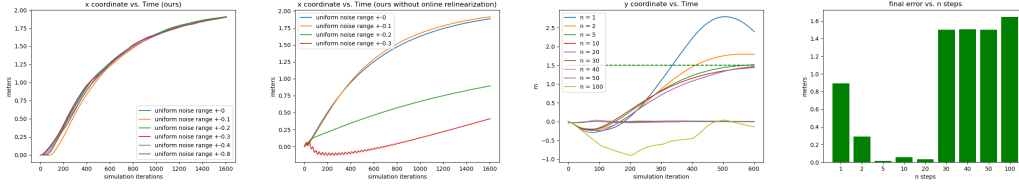


Figure 7: Left 2: The online relinearization scheme provides excellent robustness to unrealistic targets than the conventional fixed point linearization; Right 2: Simulation result and final tracking error under different relinearization timestep n

coordination. But at the same time it's to needs to pitch forward while maintaining as close as it can to the middle. Third it needs to provide enough thrust to maintain a forward velocity. As one sees in 5, our controller is able to handle this task. First it successfully reduces its body width for over 30%, and secondly it did so while maintaining balance, allowing the drone to fly strictly in the forward with no more than 5 cm deviation in the z over the 8 second, as seen in Figure 6 bottom.

Online Relinearization vs. Fixed Point In this section, we show our method's superior robustness over the traditional fixed point optimization scheme. In the experiment shown in Figure 7, both control methods are presented with an approximate fixed point that is pre-obtained. We will initialize both controllers with this fixed point as the target to reach, with no perturbation added to it, and it can be seen that both controllers yield comparable control quality. Then we apply random uniform noise to each entry of the fixed point, increasingly from 10% to 80%. We observe that the fixed point approach starts to break down at 20% noise level, and it starts to generate NaNs from 40% noise level. In contrast, our method receives no degradation in quality even when its target is corrupted by 80% noise. This is an important virtue as it vastly relieves the burden from human to devise precise and feasible target-actuation pairs.

Influence of linearized frequency n on control efficacy One crucial hyperparameter choice in this system is the frequency at which the non-linear dynamics is linearized, which presents a trade-off between the higher precision in dynamics and the extra computational overhead. Besides, the linearization frequency is coupled with the kp gain, which determines the "step size" towards the target. In this regard, large n combined with large kp gains, vs. small n combined with small kp gains embodies different behaviors. The former sets long-term goals, which tends it to decelerate and stop for each target; the latter is constantly setting new goals, causing it to always chase after something further ahead. Although the former is supposedly sub-optimal, it also implies better stability. In this experiment we investigate in the difference in behavior by trying multiple values of n from 1 to 100 in the task stabilize a soft drone at $(0, 1.5, 0)$. As shown in Figure 7, the results deem 5, 10 and 20 to be the most favorable parameters. As we have expected, controlling with overly small n leads to aggressive overshoots, while controlling with n too large leads to inadequate behaviors.

6 Limitation and Conclusion

To conclude, we proposed the first computational system to generate controllers for various types of soft multicopters with different geometries and dynamics. Our algorithm can be automatically incorporated into an enhanced LQR controller to generate robust control policies to conduct soft multicopters to perform a variety of tasks, as shown in our results section. We want to highlight that our algorithm relies on conventional IMU sensing and LQR control techniques, without using any advanced soft sensing or deeping network training techniques, which builds a bridge between the communities of soft and rigid drone. There are several limitations of our current approach. First, the sensor and propeller layout were not generated manually. In the future work we plan to automate this process. Second, every drone requires specific model training to embed geometric priors into the network. In the next step, we aim to develop a unified model that can adapt to different geometries. Third, we used pair of propellers to cancel the spinning torque effects on a drone body, which complicates the manufacturing process. In the future, we plan to conduct evaluations on real 3D printed soft multicopters to explore the potential gap between virtual simulation and real-world experiments.

References

- [1] D. Rus and M. T. Tolley. Design, fabrication and control of soft robots. *Nature*, 521(7553): 467–475, 2015.
- [2] C. Lee, M. Kim, Y. J. Kim, N. Hong, S. Ryu, H. J. Kim, and S. Kim. Soft robot review. *International Journal of Control, Automation and Systems*, 15(1):3–15, 2017.
- [3] C. M. Best, M. T. Gillespie, P. Hyatt, L. Rupert, V. Sherrod, and M. D. Killpack. A new soft robot control method: Using model predictive control for a pneumatically actuated humanoid. *IEEE Robotics Automation Magazine*, 23(3):75–84, 2016.
- [4] Z. Shen, J. Yi, X. Li, M. H. P. Lo, M. Z. Chen, Y. Hu, and Z. Wang. A soft stretchable bending sensor and data glove applications. *Robotics and biomimetics*, 3(1):22, 2016.
- [5] H. Yang, D. Qi, Z. Liu, B. K. Chandran, T. Wang, J. Yu, and X. Chen. Soft thermal sensor with mechanical adaptability. *Advanced Materials*, 28(41):9175–9181, 2016.
- [6] T. V. Quoc, H. N. Dac, T. P. Quoc, D. N. Dinh, and T. C. Duc. A printed circuit board capacitive sensor for air bubble inside fluidic flow detection. *Microsystem Technologies*, 21(4):911–918, 2015.
- [7] R. Tedrake. Underactuated robotics: Algorithms for walking, running, swimming, flying, and manipulation (course notes for mit 6.832), downloaded on 7, 19, 2020 from <http://underactuated.mit.edu/>.
- [8] K. Agrawal and P. Shrivastav. Multi-rotors: A revolution in unmanned aerial vehicle. *International Journal of Science and Research*, 4(11):1800–1804, 2015.
- [9] A. Tayebi and S. McGilvray. Attitude stabilization of a four-rotor aerial robot. In *2004 43rd IEEE Conference on Decision and Control (CDC)(IEEE Cat. No. 04CH37601)*, volume 2, pages 1216–1221. Ieee, 2004.
- [10] D. Mellinger and V. Kumar. Minimum snap trajectory generation and control for quadrotors. In *2011 IEEE international conference on robotics and automation*, pages 2520–2525. IEEE, 2011.
- [11] G. Hoffmann, H. Huang, S. Waslander, and C. Tomlin. Quadrotor helicopter flight dynamics and control: Theory and experiment. In *AIAA guidance, navigation and control conference and exhibit*, page 6461, 2007.
- [12] T. Du, A. Schulz, B. Zhu, B. Bickel, and W. Matusik. Computational multicopter design. 2016.
- [13] S. Bouabdallah, A. Noth, and R. Siegwart. Pid vs lq control techniques applied to an indoor micro quadrotor. In *2004 IEEE/RSJ International Conference on Intelligent Robots and Systems (IROS)(IEEE Cat. No. 04CH37566)*, volume 3, pages 2451–2456. IEEE, 2004.
- [14] S. L. Waslander, G. M. Hoffmann, J. S. Jang, and C. J. Tomlin. Multi-agent quadrotor testbed control design: Integral sliding mode vs. reinforcement learning. In *2005 IEEE/RSJ International Conference on Intelligent Robots and Systems*, pages 3712–3717. IEEE, 2005.
- [15] Z. Wang, K. Akiyama, K. Nonaka, and K. Sekiguchi. Experimental verification of the model predictive control with disturbance rejection for quadrotors. In *2015 54th Annual Conference of the Society of Instrument and Control Engineers of Japan (SICE)*, pages 778–783. IEEE, 2015.
- [16] J. Xu, T. Du, M. Foshey, B. Li, B. Zhu, A. Schulz, and W. Matusik. Learning to fly: computational controller design for hybrid uavs with reinforcement learning. *ACM Transactions on Graphics (TOG)*, 38(4):1–12, 2019.
- [17] M. Zhao, F. Shi, T. Anzai, K. Chaudhary, X. Chen, K. Okada, and M. Inaba. Flight motion of passing through small opening by dragon: Transformable multilinked aerial robot. In *2018 IEEE/RSJ International Conference on Intelligent Robots and Systems (IROS)*, pages 4735–4742. IEEE, 2018.

- [18] M. Zhao, K. Kawasaki, T. Anzai, X. Chen, S. Noda, F. Shi, K. Okada, and M. Inaba. Transformable multirotor with two-dimensional multilinks: Modeling, control, and whole-body aerial manipulation. *The International Journal of Robotics Research*, 37(9):1085–1112, 2018.
- [19] D. Floreano, S. Mintchev, and J. Shintake. Foldable drones: from biology to technology. In *Bioinspiration, Biomimetics, and Bioreplication 2017*, volume 10162, page 1016203. International Society for Optics and Photonics, 2017.
- [20] M. Kulkarni, H. Nguyen, and K. Alexis. The reconfigurable aerial robotic chain: Shape and motion planning. *arXiv preprint arXiv:1911.10627*, 2019.
- [21] T. Anzai, M. Zhao, S. Nozawa, F. Shi, K. Okada, and M. Inaba. Aerial grasping based on shape adaptive transformation by halo: Horizontal plane transformable aerial robot with closed-loop multilinks structure. In *2018 IEEE International Conference on Robotics and Automation (ICRA)*, pages 6990–6996. IEEE, 2018.
- [22] T. George Thuruthel, Y. Ansari, E. Falotico, and C. Laschi. Control strategies for soft robotic manipulators: A survey. *Soft robotics*, 5(2):149–163, 2018.
- [23] T. M. Bieze, F. Largilliere, A. Kruszewski, Z. Zhang, R. Merzouki, and C. Duriez. Finite element method-based kinematics and closed-loop control of soft, continuum manipulators. *Soft robotics*, 5(3):348–364, 2018.
- [24] G. Urbain, J. Degraeve, B. Carette, J. Dambre, and F. Wyffels. Morphological properties of mass-spring networks for optimal locomotion learning. *Frontiers in neurorobotics*, 11:16, 2017.
- [25] P. Battaglia, R. Pascanu, M. Lai, D. J. Rezende, et al. Interaction networks for learning about objects, relations and physics. In *Advances in neural information processing systems*, pages 4502–4510, 2016.
- [26] A. Spielberg, A. Zhao, Y. Hu, T. Du, W. Matusik, and D. Rus. Learning-in-the-loop optimization: End-to-end control and co-design of soft robots through learned deep latent representations. In *Advances in Neural Information Processing Systems*, pages 8284–8294, 2019.
- [27] B. Kim, S. B. Lee, J. Lee, S. Cho, H. Park, S. Yeom, and S. H. Park. A comparison among neo-hookean model, mooney-rivlin model, and ogden model for chloroprene rubber. *International Journal of Precision Engineering and Manufacturing*, 13(5):759–764, 2012.
- [28] B. Skallerud and B. Haugen. Collapse of thin shell structures stress resultant plasticity modelling within a co-rotated andes finite element formulation. *International Journal for Numerical Methods in Engineering*, 46(12):1961–1986, 1999.
- [29] D. Terzopoulos and A. Witkin. Physically based models with rigid and deformable components. *IEEE Computer Graphics and Applications*, 8(6):41–51, 1988.
- [30] A. Pentland and J. Williams. Good vibrations: Modal dynamics for graphics and animation. In *Proceedings of the 16th annual conference on Computer graphics and interactive techniques*, pages 215–222, 1989.
- [31] O. Sorkine and M. Alexa. As-rigid-as-possible surface modeling. In *Proceedings of the fifth Eurographics symposium on Geometry processing*, pages 109–116, 2007.
- [32] W. Lu, N. Jin, and R. Fedkiw. Two-way coupling of fluids to reduced deformable bodies. In *Proceedings of the ACM SIGGRAPH/Eurographics Symposium on Computer Animation*, pages 67–76, 2016.
- [33] K. He, X. Zhang, S. Ren, and J. Sun. Deep residual learning for image recognition. In *2016 IEEE Conference on Computer Vision and Pattern Recognition (CVPR)*, pages 770–778, 2016.
- [34] E. Weinan. A proposal on machine learning via dynamical systems. *Communications in Mathematics and Statistics*, 5(1):1–11, 2017.

- [35] Y. Lu, A. Zhong, Q. Li, and B. Dong. Beyond finite layer neural networks: Bridging deep architectures and numerical differential equations. In *International Conference on Machine Learning*, pages 3276–3285, 2018.
- [36] H. Si. Tetgen, a delaunay-based quality tetrahedral mesh generator. *ACM Trans. Math. Softw.*, 41(2), Feb. 2015. ISSN 0098-3500. doi:10.1145/2629697. URL <https://doi.org/10.1145/2629697>.
- [37] F. L. Markley, Y. Cheng, J. L. Crassidis, and Y. Oshman. Averaging quaternions. *Journal of Guidance, Control, and Dynamics*, 30(4):1193–1197, 2007.
- [38] M. Müller and M. H. Gross. Interactive virtual materials. In *Graphics interface*, volume 2004, pages 239–246, 2004.
- [39] J. Barbič and J. Popović. Real-time control of physically based simulations using gentle forces. *ACM transactions on graphics (TOG)*, 27(5):1–10, 2008.
- [40] P. Foehn and D. Scaramuzza. Onboard state dependent lqr for agile quadrotors. In *2018 IEEE International Conference on Robotics and Automation (ICRA)*, pages 6566–6572. IEEE, 2018.
- [41] E. Kaufmann, A. Loquercio, R. Ranftl, A. Dosovitskiy, V. Koltun, and D. Scaramuzza. Deep drone racing: Learning agile flight in dynamic environments. *arXiv preprint arXiv:1806.08548*, 2018.

Soft Multicopter Control using Neural Dynamics Identification Supplementary

A Overview

In this document we present the supplementary materials to our submitted paper. In Section 2, we describe the specifications of the 2D and 3D drone models used in our training and testing, including the soft material properties as well as the rotor and sensor placements. In Section 3 we introduce how the sensor measurements are converted to the state vectors s and e we used in the dynamics formulation, and propose a general guideline for inserting IMU sensors for arbitrary drone shapes. In Section 4 we describe the simulation environment, the simulation model used and the noise treatment. In Section 5, we specify the details about the learning module, including the network structure used, data generation scheme, as well as techniques and hyperparameters utilized in the training procedure; in the section we also present and discuss further testing results regarding the efficacy of network system identification. In Section 6, we specify the parameters used in our control module and the mathematical models for the LQR controller used as benchmark. In the last section, we discussed the reality gap, the design choices, and the simulation assumptions we made toward the fabrication of a real soft multicopter.

B Drone Designs

Geometry and material In our work, the s and e vector which jointly defines the soft drone’s deformation will be measured by Inertial Measurement Units only. In this section we will introduce how these sensors are employed for our examples. In section 2, we will further discuss the general rules for sensor placement. For the 3D examples, the sensing scheme is depicted in Figure 8. Each IMU is able to output the rotation information of itself as a rigid object, which is attached to a local region on the surface of the drone. In other words it defines its own reference frame with its X,Y,Z axes. On the figure, the X, Y, Z axes are coded by Red, Green, Blue respectively, with the Y axes pointing out of the plane. Each measurement will be done by an individual IMU, and for the peripheral measurements we will only make use of the measured Y axis neglecting the X and Z axes. Since rotation in 2D can be represented by one scalar only, for 2D drones the ”IMU” will only output the angle between the measured vector and the horizontal. The measured vectors are depicted in Figure 9. The specifications of our models tested are presented in Table. 1.

To customize 2D drones, we developed a web-based painting tool to sketch contours; then we use TetGen[36] to create triangle meshes from the contours. The interface also allows users to set rotor positions and assign materials to triangle elements of the mesh by drawing. 10. 3D drones are modeled in Maya and then converted to tetrahedron meshes using TetGen.

Dual-Propeller Rotor A rotor mounted on a soft drone will influence the drones body with

1. the thrust from accelerating the air and creating a low pressure region in front of it, a force which will act in the normal direction of the surface on which the rotor is mounted;
2. the torque that acts on the drone’s body in the opposite direction of the rotor’s rotation to conserve angular momentum;
3. the gyroscopic torque that will act in the direction perpendicular to the gravity and the rotor’s spinning direction, which happens when the rotor is tilted.

In this work, each of the k actuators will be implemented by a dual-rotor with counter rotation, and the actuation will be split in half for each of the two rotors. With the two sub-rotors spinning in countering directions, the second term will be cancelled out. The two sub-rotors will cancel the

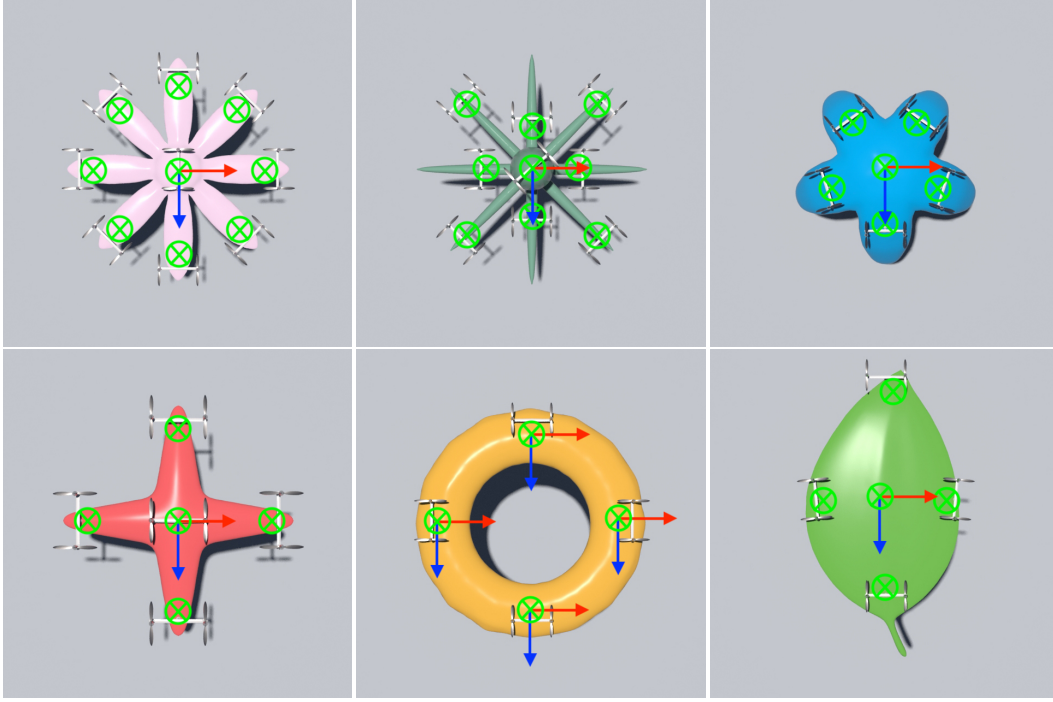


Figure 8: Drone's sensor placement (3D). Top row: Flower, Octopus, Orange Peel; Bottom row: Starfish, Donut, Leaf.

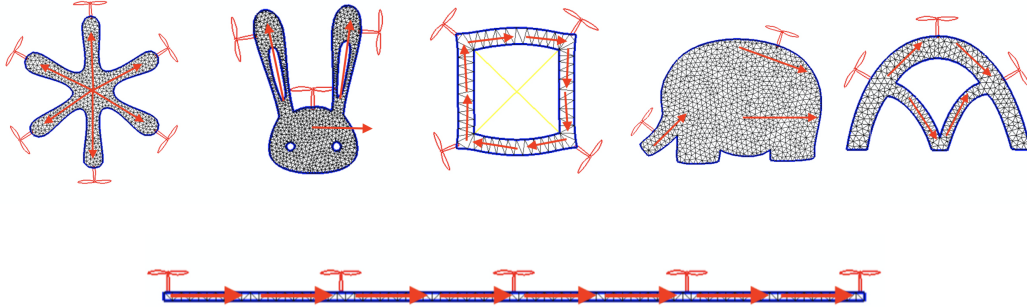


Figure 9: Drone's sensor placement for 2D designs (illustrated by red arrows). Top row: Engine, Bunny, Diamond, Elephant, Rainbow; Bottom row: Long Rod.

gyroscopic moments of there counterparts as well. Under this setting, in our simulation only the normal force is modelled.

C IMU Sensors

An Inertial Measurement Unit (IMU) combines the readings of accelerometers, gyroscopes and magnetometers to approximate the rate of rotation and the current rotation, in the form of Euler angles, rotation matrices or quaternions.

The first task is to obtain e to define the body frame of the deformable drone. In the common case where the drone's body contains no hole in the middle, an IMU will be placed at the geometric center, and the measured rotation of the IMU's rigid frame will be used as the definition of the drone's body frame. For cases like Example.x, where there is a hole in the middle, the strategy is to insert a few IMU at the circumferential locations, and average these obtained rotations. In our case where the 4 inserted IMUs are point-symmetric, the average rotation is obtained by averaging the

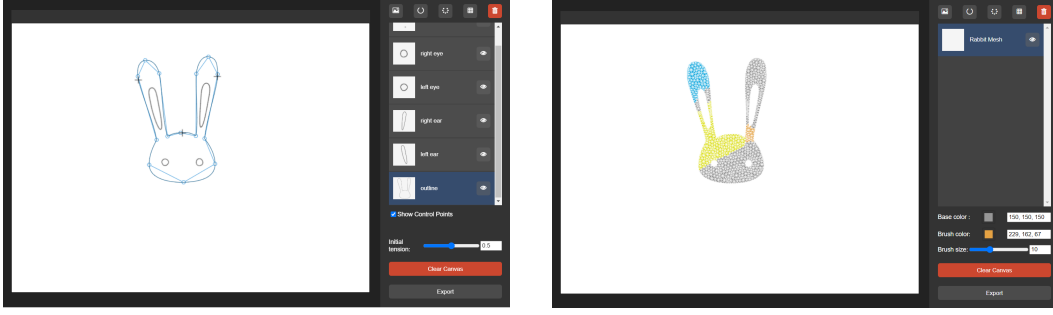


Figure 10: Left: sketching the contour; Right: painting the mesh.

3D models						
specs	Donut	Starfish	Flower	Leaf	Octopus	Orange peel
mass(kg)	1	1	1	1	1	1
modulus(N/m^2)	1e4	3e3	6e3	3e3	1e4	5e2
length-x(m)	3.5	3.6	3.6	2.4	3.6	3
length-y(m)	0.36	0.375	0.225	0.075	1.5	1.3
length-z(m)	3.5	3.6	3.6	4.5	3.6	2.9
num sensors	4	4	8	4	8	5
num rotors	4	5	9	4	9	5
max thrust(N)	10	10	10	10	10	10

2D models						
specs	Engine	Bunny	Diamond	Elephant	Rainbow	Long Rod
mass(kg)	1	1	1	1	1	1
modulus(N/m^2)	6e3	6e3	6e3	6e3	6e3	6e3
length-x(m)	1.90	1.12	1.47	2.46	2.08	0.1
length-y(m)	2.16	1.75	1.42	1.69	1.30	8.0
num sensors(m)	6	3	8	3	4	8
num rotors(m)	6	3	4	2	2	5
max thrust(N)	10	10	10	10	10	10

Table 1: Design Specifications

body-frame x direction of IMU 1, 3, the body-frame y direction of IMU 2,4, and use cross product to obtain the combined body frame. For the general case, this operation can be done by converting these measurements into quaternions and apply the averaging methods described in [37] to obtain the body frame.

The deformation vector s will constitute of measurements from IMUs inserted at peripheral points. We present a general guideline for selecting these points in the left part of Figure 11. Given an arbitrary drone shape in 3D (pressed onto the X-Z plane), we build a tree with the root node being the geometric center of the drone, and the child nodes being the rotors. The IMUs will be inserted at the edges of the tree near the outer rotor. The effectiveness of this approach is contingent to the simple modality of the soft drone’s deformation. For instance, if you take a look at the right part of Figure 11, for the above case, the deformed shape of the drone’s arm can be approximately reconstructed from the three measurements, whereas in the lower case, the three measurements are far from enough to describe the deformed shape, as the deformation is highly multi-modal, while these higher order deformation modes are effectively beyond the controlling capacity of the drone’s rotors. As a result, it is the task in the design of these drones (mostly in the modulus and thickness) so that the drone is soft enough to perform significant deformation, while deformation mode of the drone is simple. In practice, this IMU insertion guideline works for our various examples.

For the measuring these local deformations, we will measure the normal vector of the local body surface, which is the direction of the Y-axis of IMU’s body frame. Given the IMU’s measured

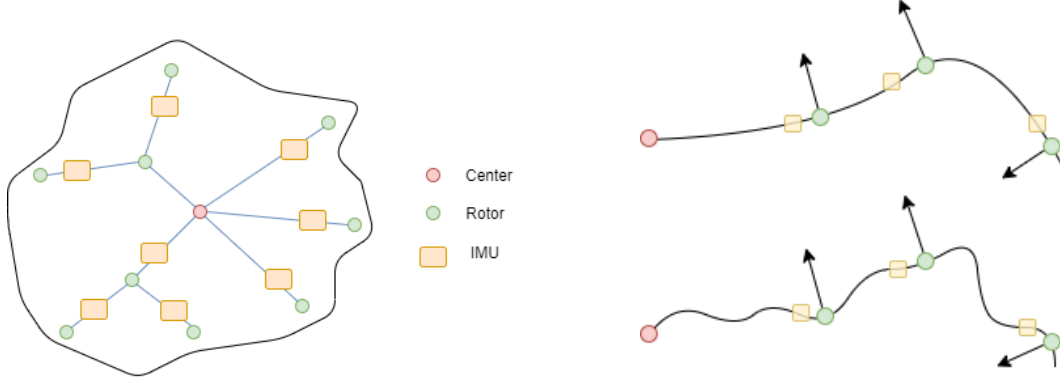


Figure 11: IMU placement. The left figure describes the proposed scheme for inserting IMUs for drones with arbitrary, irregular geometries. The right illustrates the different level of adequacy of this scheme at two different levels of softness.

rotation matrix (body-to-world) $\mathbf{R}_{peripheral}$, we will first calculate its Y-axis in the world frame by

$$\mathbf{y}_w = \mathbf{R}_{peripheral} \begin{bmatrix} 0 \\ 1 \\ 0 \end{bmatrix}. \quad (7)$$

Then given the body-to-world rotation matrix $\mathbf{R}_{central}$ defined by \mathbf{e} , we will map the \mathbf{y}_w on to the drone's body frame:

$$\mathbf{y}_b = \mathbf{R}_{central}^T \mathbf{y}_w \quad (8)$$

Then, an axis-angle will be calculated for how to rotate the Y-axis in the drone's body frame to \mathbf{y}_b . The axis will be calculated by:

$$\mathbf{v} = \mathbf{y}_b \times \begin{bmatrix} 0 \\ 1 \\ 0 \end{bmatrix} \quad (9)$$

$$\hat{\mathbf{v}} = \frac{\mathbf{v}}{\|\mathbf{v}\|} \quad (10)$$

The angle will be calculated by:

$$\alpha = \beta \cdot \arccos\left(\frac{\mathbf{y}_b}{\|\mathbf{y}_b\|} \cdot \begin{bmatrix} 0 \\ 1 \\ 0 \end{bmatrix}\right) \quad (11)$$

where

$$\beta = \begin{cases} 1 & \text{if } \hat{\mathbf{v}} \times \mathbf{r} \text{ has positive x-entry} \\ -1 & \text{if } \hat{\mathbf{v}} \times \mathbf{r} \text{ has negative x-entry} \end{cases}, \quad (12)$$

with \mathbf{r} representing the body frame location of the inserted IMU when undeformed.

In this way, the deformation is converted into a scalar, and by the construction of β , the magnitude of the scalar will represent the magnitude of the deformation, while the sign represents whether the deformation is inward (positive) or outward (negative).

In simulation environment, an IMU is implemented by binding a number of nearby vertices and use their positions to define a reference frame via cross products.

D Environment

D.1 Soft Body Model

In our testing environment, the deformation of a soft body is simulated using an explicit co-rotated elastic finite element model [38]. A mass-proportional damping term is used to model the damped

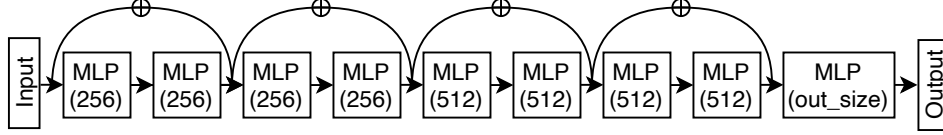


Figure 12: Network architecture: This architecture is similar to ResNet. Here each MLP consists of a fully connected layer and a ReLU except the last layer. The number in the parentheses means output dimension of each layer.

elastic behavior. We use tetrahedron (3D) and triangle (2D) meshes for discretization. An OpenMP-based parallel implementation of the elastic solver was employed to boost the simulation performance. Each rotor is rigidly bound to a local set of surface vertices on the finite element mesh in the course of simulation, with the rotor direction aligned to the averaged normal direction of the local surface triangle primitives in 3D (surface segments in 2D).

D.2 Noise Treatment

In the simulation environment, in order to emulate the perturbations and uncertainties in the real world, noise is added to the sensor readings, and a time delay is added to the rotor output. The details of these noise is given in the table below.

Category	Noise type	Level
angle measurements	Gaussian	$\mu = 0, \sigma = 0.573^\circ$
position measurements	Gaussian	$\mu = 0, \sigma = 0.01m$
rotor perturbation	Gaussian	$\mu = 0, \sigma = 0.1N$
output delay	constant	$0.03s$

E Neural-Networks

E.1 Dataset Generation

The training data are generated with our implementation of a Finite Element simulator. Given a drone geometry, we initialize the drone as undeformed, lying at the origin, and apply a random thrust to each rotor and observe the drone’s position, rotation and deformation at 100 Hz. Each set of random thrust is applied for 0.6 seconds. Other data generation schemes we tried also consist of using a rigid LQR controller to generate the thrusts, or apply a different random thrust each frame, but the former yields poor test loss due to the confined distribution of LQR control outputs, while the latter were too noisy to train. The insight is that we need to give the system enough time to respond to a signal and display meaningful behavior.

E.2 Network Architecture and Training

As shown in Figure 12, All the three neural networks to learn $\{\mathbf{d}, \mathbf{g}, \mathbf{h}\}$ follows the same architecture. The architecture is similar to ResNet except that the convolution layers are replaced by fully connected layers. Note that there is no normalization techniques used in our networks. We use Adam optimizer with initial learning rate 0.001 and decay rate 0.8 for each 20 steps. The batch size is 512. We train for 50 epoches. For loss function we found out L1 loss provides superior result to L2 loss due to the robustness of the L1 loss.

E.3 Testing of the Networks

Our networks predicts the temporal evolution of the rate of change of the three state vectors \mathbf{s} , \mathbf{e} , and \mathbf{p} . A straightforward way of testing a network’s performance is to compare its prediction to the ground truth, which will come from the test set which the network has not encountered during training. The top row of Figure. 13 depicts the results of such testing done for the *starfish* model. Since the ground truth in orange and the prediction in blue are mostly overlaid, it is clear that our training is successful. However, the mere fact that the predicted rates of change are visually

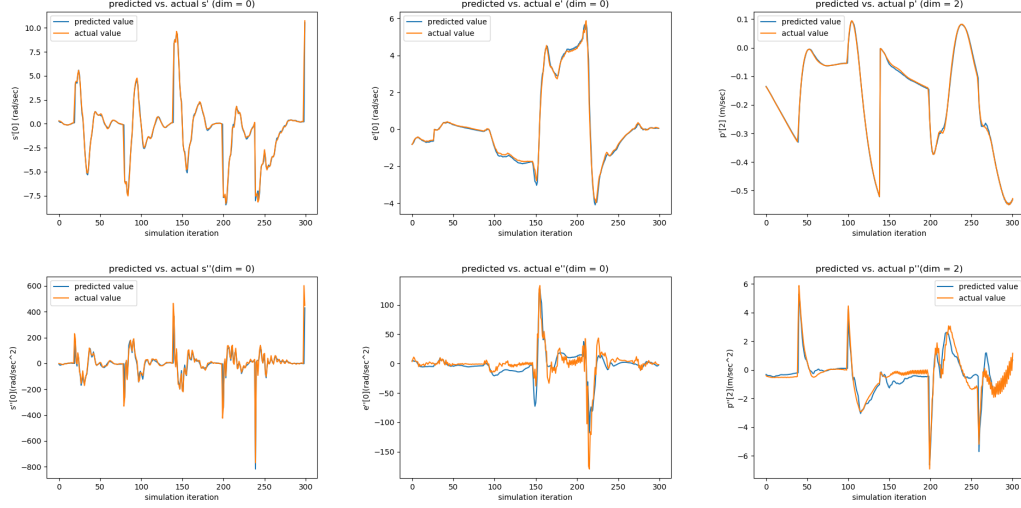


Figure 13: Testing results of the networks

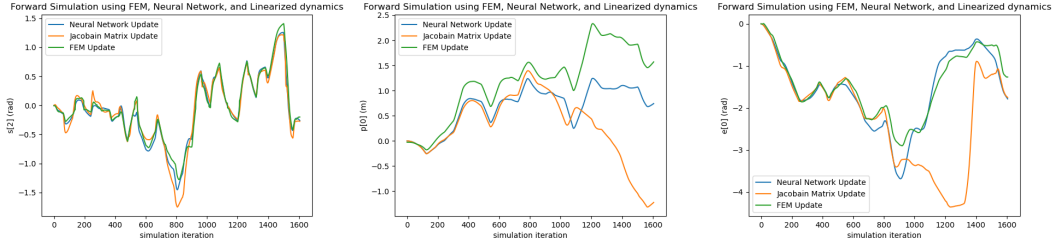


Figure 14: Testing results of the Network Linearization

close to the ground truth, doesn't necessarily entail that the network is going to work, because the network takes the last frame's rate of change as its input, so even if it fails to recognize the dynamics of the system, as long as it learns to stay close to that input, the resulting curves will look good. As a result, what we actually care about in testing these networks, is whether it correctly predicts the dynamics of the rate of change — the acceleration. The bottom row depicts the predicted acceleration corresponding to the first row's velocity, obtained by taking the difference between the current rate of change and the last rate of change. We can see that in our case, the acceleration is successfully learned by the network in an implicit fashion.

Only testing the network's forward dynamics is not enough either, since the LQR doesn't take in the network parameters. What it uses is the Taylor Expansion the network, which are made up of the gradients with respect to its inputs. Since it is actually the gradient that matters, we cannot merely treat the networks as black-box functions providing the input-output mappings. In other words, from the network the LQR not only expects it to approximate the output from its inputs, but also do it in the right manner. Besides, we need to make sure that the function contour is not erratically bumpy, so that it is reasonable to approximate the function locally using linear approximations. For this purpose, we conduct a test case where we generate a sequence of 1600 frames from the FEM simulator using random thrust signals. Then we roll out the same simulation using the linearized equation

$$\dot{\mathbf{x}} = \mathbf{f}(\mathbf{x}, \mathbf{u}) \approx \mathbf{f}(\mathbf{x}^*, \mathbf{u}^*) + \mathbf{A}(\mathbf{x} - \mathbf{x}^*) + \mathbf{B}(\mathbf{u} - \mathbf{u}^*), \quad (13)$$

which is Equation. 13 in the paper, which represents the system that the LQR sees. Here, the linearization is done at 20 Hz. With the plots in Figure. 14 we show that even with the error accumulation in the roll-out, the linearized system is able to keep up with the ground truth provided by the high-fidelity FEM simulation for around 1000 frames, *i.e.* 20 seconds. This shows that our attempt to control the non-linear dynamics based on the linearizations of the neural networks is on solid grounds.

F Control

F.1 LQR Overview

The Linear Quadratic Controller is a kind of full-state feedback controller, where the control of the system is based on the current state. Given a linear system in state space form:

$$\dot{\mathbf{x}} = \mathbf{A}\mathbf{x} + \mathbf{B}\mathbf{u} \quad (14)$$

where \mathbf{x} is the state vector, \mathbf{u} is the control vector (in our case the thrusts for individual propellers), and \mathbf{A} and \mathbf{B} are matrices, we compute a control matrix \mathbf{K} and combine that with the state by:

$$\mathbf{u} = -\mathbf{K}\mathbf{x} \quad (15)$$

The way we \mathbf{K} is as follows: Suppose we want to set both the state and the control to be $\mathbf{0}$. We define cost matrices \mathbf{Q} and \mathbf{R} that penalizes the \mathbf{A} squared and \mathbf{B} squared respectively, we desire to minimize the infinite horizon cost:

$$\int_0^\infty [\mathbf{x}^T \mathbf{Q} \mathbf{x} + \mathbf{u}^T \mathbf{R} \mathbf{u}] dt \quad (16)$$

which means our goal is to find the optimal cost-to-go function $\mathbf{J}^* = \mathbf{x}^T \mathbf{S} \mathbf{x}$ that satisfies the HamiltonJacobiBellman (HJB) equation. Utilizing the convex nature of the problem, we know that the minimum occurs when the gradient is zero, so we have:

$$\frac{\partial}{\partial \mathbf{t}} = 2\mathbf{u}^T \mathbf{R} + 2\mathbf{x}^T \mathbf{S} \mathbf{B} = 0 \quad (17)$$

which yields the control policy:

$$\mathbf{u} = -[\mathbf{R}^{-1} \mathbf{B}^T \mathbf{S}] \mathbf{x} = -\mathbf{K} \mathbf{x} \quad (18)$$

After transformation, we can find the value of \mathbf{S} by solving the equation:

$$\mathbf{0} = \mathbf{S} \mathbf{A} + \mathbf{A}^T \mathbf{S} - \mathbf{S} \mathbf{B} \mathbf{R}^{-1} \mathbf{B}^T \mathbf{S} + \mathbf{Q} \quad (19)$$

This is known as the **Algebraic Riccati Equation**, which can be solved by iterating backward in time.

F.2 Online Reinitialization

Although our network eliminates the necessity for the extensive, empirical parameter tuning process, there are a few hyper-parameters that needs to be tuned for effective performance. We will present the exact value or the value range for these parameters in the table below.

Parameter type	Value/Value range
\mathbf{Q} gain (related to \mathbf{s})	100 to 200
\mathbf{Q} gain (related to \mathbf{e})	50 to 200
\mathbf{Q} gain (related to \mathbf{p})	100 to 200
\mathbf{R} gain	2
kp	0.03
kd	0.0001
n	10

F.3 Rigid LQR (Benchmark) Derivation

F.3.1 State Definition

The state of a rigid object can be described by position and rotation. Let \mathbf{p} be the vector describing position, and let \mathbf{e} be the vector describing rotation. And let $\mathbf{q} = \begin{pmatrix} \mathbf{p} \\ \mathbf{e} \end{pmatrix}$. Since the dynamics is

second order, the state \mathbf{x} will be defined as $\mathbf{x} = \begin{pmatrix} \mathbf{q} \\ \dot{\mathbf{q}} \end{pmatrix}$. For the 3D case, $\mathbf{p} = \begin{pmatrix} x \\ y \\ z \end{pmatrix}$, $\mathbf{e} = \begin{pmatrix} \phi \\ \theta \\ \psi \end{pmatrix}$, where x, y, z are the spacial coordinates, ϕ, θ, ψ are Euler angles. For the 2D case, $\mathbf{p} = \begin{pmatrix} x \\ y \end{pmatrix}$, $\mathbf{e} = (\phi)$, as the rotation in 2D can be described by a sole parameter.

F.3.2 Dynamic Model

Let \mathbf{u} denote the drone's actuation, and $\mathbf{u} = \begin{pmatrix} u_1 \\ u_2 \\ \vdots \\ u_k \end{pmatrix}$, where k is the number of propellers and

u_i represents the thrust provided by each propeller. The dynamic model is a function \mathbf{f} such that $\dot{\mathbf{x}} = \mathbf{f}(\mathbf{x}, \mathbf{u})$. In 3D, the dynamics of the drone will be directly derived from the Newton-Euler equations:

$$m\ddot{\mathbf{p}} = m\mathbf{g} + \mathbf{R}\mathbf{M}_f\mathbf{u} \quad (20)$$

$$\mathbf{J}(\dot{\mathbf{L}}\dot{\mathbf{e}} + \mathbf{L}\ddot{\mathbf{e}}) + (\mathbf{L}\dot{\mathbf{e}}) \times \mathbf{J}\mathbf{L}\dot{\mathbf{e}} = \mathbf{M}_t\mathbf{u} \quad (21)$$

with the variable definitions given in the table below. For the 2D case, these equations simplifies to

$$m\ddot{\mathbf{p}} = m\mathbf{g} + \mathbf{R}\mathbf{M}_f\mathbf{u} \quad (22)$$

$$\mathbf{J}\ddot{\mathbf{e}} = \mathbf{M}_t\mathbf{u} \quad (23)$$

\mathbf{R}	$\text{SO}(3)$	Body-to-world rotation matrix
\mathbf{r}	R^3	Motor position in body frame
\mathbf{d}	unit sphere	Motor orientation in body frame
\mathbf{M}_f	$R^{3 \times n}$	Mapping from thrusts to net force. The i -th column is \mathbf{d}_i .
\mathbf{M}_t	$R^{3 \times n}$	Mapping from thrusts to net torque. The i -th column is $bi\lambda i\mathbf{d}_i + r_i \times \mathbf{d}_i$
\mathbf{J}	R^3	Inertia Tensor in Body Frame. Value is $\begin{bmatrix} I_{xx} & I_{xy} & I_{xz} \\ I_{yx} & I_{yy} & I_{yz} \\ I_{zx} & I_{zy} & I_{zz} \end{bmatrix}$
I_{xx}	R	$\sum_i m_i * (y_i^2 + z_i^2)$
I_{yy}	R	$\sum_i m_i * (z_i^2 + x_i^2)$
I_{zz}	R	$\sum_i m_i * (x_i^2 + y_i^2)$
I_{xy}	R	$-\sum_i m_i * x_i * y_i$
I_{xz}	R	$-\sum_i m_i * x_i * z_i$
I_{yz}	R	$-\sum_i m_i * y_i * z_i$
\mathbf{L}	R^3	Mapping from world frame angular velocity to body frame angular velocity, such that $\omega = \mathbf{L}\dot{\mathbf{e}}$. Value is $\begin{bmatrix} 1 & 0 & -s(\theta) \\ 1 & c(\theta) & s(\phi)c(\theta) \\ 1 & -s(\phi) & c(\phi)c(\theta) \end{bmatrix}$
$\dot{\mathbf{L}}$	R^3	Derivative of \mathbf{L} . Value is $\begin{bmatrix} 0 & 0 & -c(\theta)\dot{\theta} \\ 1 & -s(\phi)\dot{\phi} & c(\phi)c(\theta)\dot{\phi} - s(\phi)s(\theta)\dot{\theta} \\ 1 & -c(\phi)\dot{\phi} & s(\phi)c(\theta)\dot{\phi} - c(\phi)s(\theta)\dot{\theta} \end{bmatrix}$

Manipulator Form Follow the formulation purposed in [7], we will reorganize these equations into the Manipulator Form, whose template is as follows:

$$\mathbf{H}(\mathbf{q})\ddot{\mathbf{q}} + \mathbf{C}(\mathbf{q}, \dot{\mathbf{q}})\dot{\mathbf{q}} + \mathbf{G}(\mathbf{q}) = \mathbf{B}(\mathbf{q})\mathbf{u}, \quad (24)$$

Consequently,

$$\ddot{\mathbf{q}} = \mathbf{H}^{-1}(\mathbf{B}(\mathbf{q})\mathbf{u} - \mathbf{C}(\mathbf{q}, \dot{\mathbf{q}})\dot{\mathbf{q}} - \mathbf{G}(\mathbf{q})) \quad (25)$$

This allows us to write:

$$\mathbf{f}(\mathbf{x}, \mathbf{u}) = \dot{\mathbf{x}} = \begin{bmatrix} \dot{\mathbf{q}} \\ \dot{\mathbf{q}} \end{bmatrix} = \begin{bmatrix} \mathbf{H}^{-1}(\mathbf{B}(\mathbf{q})\mathbf{u} - \mathbf{C}(\mathbf{q}, \dot{\mathbf{q}})\dot{\mathbf{q}} - \mathbf{G}(\mathbf{q})) \end{bmatrix} \quad (26)$$

For the 3D case, reorganizing the dynamics equations yields $\mathbf{H} = \begin{bmatrix} m\mathbf{I}_3 & \mathbf{O} \\ \mathbf{O} & \mathbf{J}\mathbf{L} \end{bmatrix}$, $\mathbf{C} = \begin{bmatrix} \mathbf{O} & \mathbf{O} \\ \mathbf{O} & \mathbf{J}\dot{\mathbf{L}} + \mathbf{L}\dot{\mathbf{e}} \times \mathbf{J}\mathbf{L} \end{bmatrix}$, $\mathbf{G} = \begin{bmatrix} -mg \\ \mathbf{O} \end{bmatrix}$, $\mathbf{B} = \begin{bmatrix} \mathbf{R}\mathbf{M}_f \\ \mathbf{M}_t \end{bmatrix}$.

For the 2D case, we have $\mathbf{H} = \begin{bmatrix} m\mathbf{I}_2 & \mathbf{O} \\ \mathbf{O} & \mathbf{J} \end{bmatrix}$, $\mathbf{C} = [\mathbf{O}]$, $\mathbf{G} = \begin{bmatrix} -mg \\ \mathbf{O} \end{bmatrix}$, $\mathbf{B} = \begin{bmatrix} \mathbf{R}\mathbf{M}_f \\ \mathbf{M}_t \end{bmatrix}$.

F.3.3 Linearization via Taylor Expansion

Since the function $\mathbf{f}(\mathbf{x}, \mathbf{u})$ described above is a non-linear model, we will linearize it by taking the first order Taylor Expansion around an operating point $(\mathbf{x}^*, \mathbf{u}^*)$ such that $\mathbf{f}(\mathbf{x}^*, \mathbf{u}^*) = \mathbf{0}$. For \mathbf{x} close enough to \mathbf{x}^* , we have:

$$\begin{aligned} \mathbf{f}(\mathbf{x} - \mathbf{x}^*) &\approx \left(\frac{\partial \mathbf{f}}{\partial \mathbf{x}} \Big|_{\mathbf{x}=\mathbf{x}^*, \mathbf{u}=\mathbf{u}^*} \right) (\mathbf{x} - \mathbf{x}^*) + \left(\frac{\partial \mathbf{f}}{\partial \mathbf{u}} \Big|_{\mathbf{x}=\mathbf{x}^*, \mathbf{u}=\mathbf{u}^*} \right) (\mathbf{u} - \mathbf{u}^*) \\ &= \mathbf{A}_{\text{lin}}(\mathbf{x} - \mathbf{x}^*) + \mathbf{B}_{\text{lin}}(\mathbf{u} - \mathbf{u}^*) \end{aligned} \quad (27)$$

Since we know that:

$$\mathbf{f}(\mathbf{x}, \mathbf{u}) = \begin{bmatrix} \mathbf{H}^{-1}(\mathbf{B}(\mathbf{q})\mathbf{u} - \mathbf{C}(\mathbf{q}, \dot{\mathbf{q}})\dot{\mathbf{q}} - \mathbf{G}(\mathbf{q})) \end{bmatrix}, \mathbf{x} = \begin{pmatrix} \mathbf{q} \\ \dot{\mathbf{q}} \end{pmatrix}, \quad (28)$$

$\mathbf{A}_{\text{lin}} = \frac{\partial \mathbf{f}}{\partial \mathbf{x}}$ can be represented by the block matrix:

$$\begin{bmatrix} \frac{\partial \dot{\mathbf{q}}}{\partial \mathbf{q}} & \frac{\partial \dot{\mathbf{q}}}{\partial \dot{\mathbf{q}}} \\ \frac{\partial \mathbf{H}^{-1}(\mathbf{B}(\mathbf{q})\mathbf{u} - \mathbf{C}(\mathbf{q}, \dot{\mathbf{q}})\dot{\mathbf{q}} - \mathbf{G}(\mathbf{q}))}{\partial \mathbf{q}} & \frac{\partial \mathbf{H}^{-1}(\mathbf{B}(\mathbf{q})\mathbf{u} - \mathbf{C}(\mathbf{q}, \dot{\mathbf{q}})\dot{\mathbf{q}} - \mathbf{G}(\mathbf{q}))}{\partial \dot{\mathbf{q}}} \end{bmatrix} = \begin{bmatrix} \mathbf{T1} & \mathbf{T2} \\ \mathbf{T3} & \mathbf{T4} \end{bmatrix} \quad (29)$$

It can be seen trivially that $\mathbf{T1} = \frac{\partial \dot{\mathbf{q}}}{\partial \mathbf{q}} = \mathbf{O}$ and $\mathbf{T2} = \frac{\partial \dot{\mathbf{q}}}{\partial \dot{\mathbf{q}}} = \mathbf{I}_3$.

For $\mathbf{T3} = \frac{\partial \mathbf{H}^{-1}(\mathbf{B}(\mathbf{q})\mathbf{u} - \mathbf{C}(\mathbf{q}, \dot{\mathbf{q}})\dot{\mathbf{q}} - \mathbf{G}(\mathbf{q}))}{\partial \mathbf{q}}$, by the Product Rule we know,

$$\mathbf{T3} = \frac{\partial \mathbf{H}^{-1}}{\partial \mathbf{q}} (\mathbf{B}(\mathbf{q})\mathbf{u} - \mathbf{C}(\mathbf{q}, \dot{\mathbf{q}})\dot{\mathbf{q}} - \mathbf{G}(\mathbf{q})) + \mathbf{H}^{-1} \frac{\partial (\mathbf{B}(\mathbf{q})\mathbf{u} - \mathbf{C}(\mathbf{q}, \dot{\mathbf{q}})\dot{\mathbf{q}} - \mathbf{G}(\mathbf{q}))}{\partial \mathbf{q}} \quad (30)$$

Since we defined $\mathbf{x}^*, \mathbf{u}^*$ to be such that $\mathbf{f}(\mathbf{x}^*, \mathbf{u}^*) = \mathbf{0}$, then $\mathbf{H}^{-1}(\mathbf{B}(\mathbf{q})\mathbf{u} - \mathbf{C}(\mathbf{q}, \dot{\mathbf{q}})\dot{\mathbf{q}} - \mathbf{G}(\mathbf{q})) = \mathbf{0}$ at $(\mathbf{x}^*, \mathbf{u}^*)$. Since we know \mathbf{H}^{-1} is non-zero, then $\mathbf{B}(\mathbf{q})\mathbf{u} - \mathbf{C}(\mathbf{q}, \dot{\mathbf{q}})\dot{\mathbf{q}} - \mathbf{G}(\mathbf{q}) = \mathbf{0}$. Besides, since we have $\mathbf{f}(\mathbf{x}^*, \mathbf{u}^*) = \mathbf{0}$, we have $\dot{\mathbf{q}} = \mathbf{0}$, then $\frac{\partial \mathbf{C}(\mathbf{q}, \dot{\mathbf{q}})\dot{\mathbf{q}}}{\partial \mathbf{q}} = \frac{\partial \mathbf{C}(\mathbf{q}, \dot{\mathbf{q}})}{\partial \mathbf{q}} \dot{\mathbf{q}} + \mathbf{C}(\mathbf{q}, \dot{\mathbf{q}}) \frac{\partial \dot{\mathbf{q}}}{\partial \mathbf{q}} = \mathbf{0} + \mathbf{0} = \mathbf{0}$. Also, since $\mathbf{G}(\mathbf{q}) = \begin{bmatrix} -mg \\ \mathbf{O} \end{bmatrix}$, and has nothing

to do with \mathbf{q} , $\frac{\partial \mathbf{G}(\mathbf{q})}{\partial \mathbf{q}} = \mathbf{0}$. So we can conclude that:

$$\mathbf{T3} = \mathbf{H}^{-1} \frac{\partial \mathbf{B}(\mathbf{q})\mathbf{u}}{\partial \mathbf{q}} = \mathbf{H}^{-1} \left(\frac{\partial \mathbf{B}(\mathbf{q})}{\partial \mathbf{q}} \mathbf{u} + \mathbf{B}(\mathbf{q}) \frac{\partial \mathbf{u}}{\partial \mathbf{q}} \right) = \mathbf{H}^{-1} \frac{\partial \mathbf{B}(\mathbf{q})}{\partial \mathbf{q}} \mathbf{u}. \quad (31)$$

Since

$$\mathbf{B} = \begin{bmatrix} \mathbf{R}\mathbf{M}_f \\ \mathbf{M}_t \end{bmatrix} = \begin{bmatrix} \begin{pmatrix} (\mathbf{R}\mathbf{M}_f)_1 \\ (\mathbf{M}_t)_1 \end{pmatrix} & \begin{pmatrix} (\mathbf{R}\mathbf{M}_f)_2 \\ (\mathbf{M}_t)_2 \end{pmatrix} & \begin{pmatrix} (\mathbf{R}\mathbf{M}_f)_3 \\ (\mathbf{M}_t)_3 \end{pmatrix} & \begin{pmatrix} (\mathbf{R}\mathbf{M}_f)_4 \\ (\mathbf{M}_t)_4 \end{pmatrix} \end{bmatrix} \quad (32)$$

$$\frac{\partial \mathbf{B}}{\partial \mathbf{q}} = \begin{bmatrix} \frac{\partial \begin{pmatrix} (\mathbf{R}\mathbf{M}_f)_1 \\ (\mathbf{M}_t)_1 \end{pmatrix}}{\partial \mathbf{q}} & \frac{\partial \begin{pmatrix} (\mathbf{R}\mathbf{M}_f)_2 \\ (\mathbf{M}_t)_2 \end{pmatrix}}{\partial \mathbf{q}} & \frac{\partial \begin{pmatrix} (\mathbf{R}\mathbf{M}_f)_3 \\ (\mathbf{M}_t)_3 \end{pmatrix}}{\partial \mathbf{q}} & \frac{\partial \begin{pmatrix} (\mathbf{R}\mathbf{M}_f)_4 \\ (\mathbf{M}_t)_4 \end{pmatrix}}{\partial \mathbf{q}} \end{bmatrix}. \quad (33)$$

So,

$$\frac{\partial \mathbf{B}}{\partial \mathbf{q}} \mathbf{u} = \sum_i \frac{\partial \begin{pmatrix} (\mathbf{R}\mathbf{M}_f)_i \\ (\mathbf{M}_t)_i \end{pmatrix}}{\partial \mathbf{q}} * u_i, \quad (34)$$

where:

$$\begin{aligned} \frac{\partial \begin{pmatrix} (\mathbf{R}\mathbf{M}_f)_i \\ (\mathbf{M}_t)_i \end{pmatrix}}{\partial \mathbf{q}} &= \begin{bmatrix} \frac{\partial (\mathbf{R}\mathbf{M}_f)_i}{\partial \mathbf{p}} & \frac{\partial (\mathbf{R}\mathbf{M}_f)_i}{\partial \mathbf{e}} \\ \frac{\partial (\mathbf{M}_t)_i}{\partial \mathbf{p}} & \frac{\partial (\mathbf{M}_t)_i}{\partial \mathbf{e}} \end{bmatrix} = \begin{bmatrix} \mathbf{O}_{3 \times 3} & \frac{\partial \mathbf{R}}{\partial \mathbf{e}} * (\mathbf{M}_f)_i \\ \mathbf{O}_{3 \times 3} & \mathbf{O}_{3 \times 3} \end{bmatrix} \\ &= \begin{bmatrix} \mathbf{O}_{3 \times 3} & \left[\frac{\partial \mathbf{R}}{\partial \phi} * (\mathbf{M}_f)_i & \frac{\partial \mathbf{R}}{\partial \theta} * (\mathbf{M}_f)_i & \frac{\partial \mathbf{R}}{\partial \psi} * (\mathbf{M}_f)_i \right] \\ \mathbf{O}_{3 \times 3} & \mathbf{O}_{3 \times 3} \end{bmatrix}. \end{aligned} \quad (35)$$

Finally,

$$\mathbf{T}_4 = \frac{\partial \mathbf{H}^{-1}}{\partial \dot{\mathbf{q}}} (\mathbf{B}(\mathbf{q})\mathbf{u} - \mathbf{C}(\mathbf{q}, \dot{\mathbf{q}})\dot{\mathbf{q}} - \mathbf{G}(\mathbf{q})) + \mathbf{H}^{-1} \frac{\partial (\mathbf{B}(\mathbf{q})\mathbf{u} - \mathbf{C}(\mathbf{q}, \dot{\mathbf{q}})\dot{\mathbf{q}} - \mathbf{G}(\mathbf{q}))}{\partial \dot{\mathbf{q}}} = -\mathbf{H}^{-1}\mathbf{C},$$

since $\mathbf{B}(\mathbf{q})\mathbf{u} - \mathbf{C}(\mathbf{q}, \dot{\mathbf{q}})\dot{\mathbf{q}} - \mathbf{G}(\mathbf{q}) = \mathbf{0}$ and with $\dot{\mathbf{q}} = \mathbf{0}$, $\frac{\partial (\mathbf{B}(\mathbf{q})\mathbf{u} - \mathbf{C}(\mathbf{q}, \dot{\mathbf{q}})\dot{\mathbf{q}} - \mathbf{G}(\mathbf{q}))}{\partial \dot{\mathbf{q}}} = \frac{\partial (-\mathbf{C}(\mathbf{q}, \dot{\mathbf{q}})\dot{\mathbf{q}})}{\partial \dot{\mathbf{q}}} = -\mathbf{C}(\mathbf{q}, \dot{\mathbf{q}}) \frac{\partial \dot{\mathbf{q}}}{\partial \dot{\mathbf{q}}} = -\mathbf{C}(\mathbf{q}, \dot{\mathbf{q}})$.

So to sum up:

$$\mathbf{A}_{\text{lin}} = \begin{bmatrix} \mathbf{O}_{6 \times 6} & \mathbf{I}_{6 \times 6} \\ \mathbf{H}^{-1} * \sum_i \begin{bmatrix} \mathbf{O}_{3 \times 3} & \left[\frac{\partial \mathbf{R}}{\partial \phi} * (\mathbf{M}_f)_i & \frac{\partial \mathbf{R}}{\partial \theta} * (\mathbf{M}_f)_i & \frac{\partial \mathbf{R}}{\partial \psi} * (\mathbf{M}_f)_i \right] * u_i \\ \mathbf{O}_{3 \times 3} & \mathbf{O}_{3 \times 3} \end{bmatrix} & -\mathbf{H}^{-1}\mathbf{C} \end{bmatrix} \quad (36)$$

For \mathbf{B}_{lin} , we have:

$$\mathbf{B}_{\text{lin}} = \frac{\partial \mathbf{f}}{\partial \mathbf{u}} = \begin{bmatrix} \frac{\partial \dot{\mathbf{q}}}{\partial \mathbf{u}} \\ \frac{\partial \mathbf{H}^{-1}(\mathbf{B}(\mathbf{q})\mathbf{u} - \mathbf{C}(\mathbf{q}, \dot{\mathbf{q}})\dot{\mathbf{q}} - \mathbf{G}(\mathbf{q}))}{\partial \mathbf{u}} \end{bmatrix} \quad (37)$$

It is clear to see that $\frac{\partial \dot{\mathbf{q}}}{\partial \mathbf{u}} = \mathbf{0}$, and $\frac{\partial \mathbf{H}^{-1}(\mathbf{B}(\mathbf{q})\mathbf{u} - \mathbf{C}(\mathbf{q}, \dot{\mathbf{q}})\dot{\mathbf{q}} - \mathbf{G}(\mathbf{q}))}{\partial \mathbf{u}} = \frac{\partial \mathbf{H}^{-1}(\mathbf{B}(\mathbf{q})\mathbf{u})}{\partial \mathbf{u}} = \mathbf{H}^{-1}\mathbf{B}(\mathbf{q}) \frac{\partial \mathbf{u}}{\partial \mathbf{u}} = \mathbf{H}^{-1}\mathbf{B}(\mathbf{q})$, (remember that none of \mathbf{G} , \mathbf{B} , \mathbf{C} , \mathbf{H} is related to \mathbf{u}). So we have

$$\mathbf{B}_{\text{lin}} = \begin{bmatrix} \mathbf{O}_{6 \times k} \\ \mathbf{H}^{-1}\mathbf{B} \end{bmatrix} \quad (38)$$

For the 2D case \mathbf{A}_{lin} and \mathbf{B}_{lin} are simplified to become:

$$\begin{aligned} \mathbf{A}_{\text{lin}} &= \frac{\partial \mathbf{f}}{\partial \mathbf{x}} = \begin{bmatrix} \frac{\partial \dot{\mathbf{q}}}{\partial \mathbf{q}} & \frac{\partial \dot{\mathbf{q}}}{\partial \dot{\mathbf{q}}} \\ \frac{\partial \mathbf{H}^{-1}(\mathbf{B}(\mathbf{q})\mathbf{u} - \mathbf{C}(\mathbf{q}, \dot{\mathbf{q}})\dot{\mathbf{q}} - \mathbf{G}(\mathbf{q}))}{\partial \mathbf{q}} & \frac{\partial \mathbf{H}^{-1}(\mathbf{B}(\mathbf{q})\mathbf{u} - \mathbf{C}(\mathbf{q}, \dot{\mathbf{q}})\dot{\mathbf{q}} - \mathbf{G}(\mathbf{q}))}{\partial \dot{\mathbf{q}}} \end{bmatrix} \\ &= \begin{bmatrix} \mathbf{O}_{3 \times 3} & \mathbf{I}_{3 \times 3} \\ \mathbf{H}^{-1} * \sum_i \begin{bmatrix} \mathbf{O}_{2 \times 2} & \frac{\partial \mathbf{R}}{\partial \phi} * (\mathbf{M}_f)_i \\ \mathbf{O}_{1 \times 2} & \mathbf{O}_{1 \times 1} \end{bmatrix} * u_i & \mathbf{O}_{3 \times 3} \end{bmatrix} \end{aligned} \quad (39)$$

$$\mathbf{B}_{\text{lin}} = \begin{bmatrix} \frac{\partial \dot{\mathbf{q}}}{\partial \mathbf{u}} \\ \frac{\partial \mathbf{H}^{-1}(\mathbf{B}(\mathbf{q})\mathbf{u} - \mathbf{C}(\mathbf{q}, \dot{\mathbf{q}})\dot{\mathbf{q}} - \mathbf{G}(\mathbf{q}))}{\partial \mathbf{u}} \end{bmatrix} = \begin{bmatrix} \mathbf{O}_{3 \times k} \\ \mathbf{H}^{-1}\mathbf{B} \end{bmatrix} \quad (40)$$

The matrices \mathbf{A}_{lin} and \mathbf{B}_{lin} will then be optimized by the LQR to yield the control matrix \mathbf{K} . For the geometry-updating LQR, the quantities that are updated each time are \mathbf{M}_f , \mathbf{M}_t and \mathbf{J} , which are all the time-varying values in the above derivation. The fixed point is also recalculated as if it is rigid.

F.3.4 Fixed Point

Assuming $(\mathbf{x}^*, \mathbf{u}^*)$ satisfies $\mathbf{f}(\mathbf{x}^*, \mathbf{u}^*) = \mathbf{0}$, we have:

$$\mathbf{R}\mathbf{M}_f\mathbf{u}^* = -m\mathbf{g} \quad (41)$$

$$\mathbf{M}_t \mathbf{u}^* = \mathbf{0} \quad (42)$$

for torque and force balance respectively. Given certain \mathbf{M}_f , \mathbf{M}_t , we will first solve the equation:

$$\begin{bmatrix} \mathbf{1} \\ \mathbf{M}_t \end{bmatrix} \mathbf{u} = \begin{pmatrix} -\|m\mathbf{g}\| \\ \mathbf{0} \end{pmatrix} \quad (43)$$

to satisfy the torque balance. Then we will rotate the reference frame so that the direction of the combined thrust aligns with the y-axis. The rotation axis is calculated by:

$$\mathbf{v} = \mathbf{M}_f \mathbf{u}^* \times (-m\mathbf{g}) \quad (44)$$

$$\hat{\mathbf{v}} = \frac{\mathbf{v}}{\|\mathbf{v}\|} \quad (45)$$

The angle is calculated by:

$$\alpha = \frac{-m\mathbf{g}^T \mathbf{M}_f \mathbf{u}^*}{\|\mathbf{M}_f \mathbf{u}^*\| \|m\mathbf{g}\|} \quad (46)$$

After the rotation in axis-angle form is calculated, Euler angles would be extracted to form the \mathbf{e}^* part of \mathbf{x}^* .

G Toward a Real Soft Drone

Although we carried out the experiments purely in numerical simulation environments, we designed our approach with its real-life feasibility in mind, and our method is intrinsically suitable for real-world deployment. First, our perception of the soft drone is explicitly sensor based. Unlike many other works that deal with soft-robot controls like [39] [26] which observe the full state (particle positions) and apply model reduction techniques to synthesize the state, we resist this unrealistic assumption, and throughout our pipeline, the interfacing between the simulator and the training/controlling modules is strictly limited to the sensor measurements. In this sense, we observe the simulation environment in the same limited fashion as we observe the real world, so that no unfair advantage is taken. We expect the rest of the pipeline to work exactly the same if we swap the simulator with the real-world environment, since the interfacing will not be changed. Secondly, as we have mentioned in the paper, in designing the sensing scheme, the only sensors we used is a position sensor (camera or GPS, depending on application) and the Inertial Measurement Unit (IMU), which are the most basic and available tools used everywhere for rigid drones. No other sensor types, such as bending, thermal or fluidic sensors are used. This simplistic approach allows us to conveniently fabricate these soft drones by implanting the IMU microprocessors at the surface, without having to cut open the drone's body or insert extra measurement devices. Basically, to fabricate an actual soft drone, we just need to cut out the desired shape from solid materials (if not with 3D printing techniques), implant the IMUs at the surface, set up their connection to a central onboard processor using WIFI, and flash the trained neural network and controlling script onto the hardware. Thirdly, the computational efficiency of our algorithm allows us it to be handled by on-board processors. In the testing case, our relinearization is done at 10Hz, and can be relaxed to 20Hz for the more stable geometries. There have been previous works conducted that performs LQR recalculation [40] and network based control loop [41] at 10Hz using onboard computers. With further code optimization, we believe that our current system can be implemented fully onboard. Lastly, we simulate the soft body using a co-rotated elastic Finite Element simulator, which is well-known for providing physically realistic behaviours and is commonly used in engineering design, with noise and time delay applied. As a result, our success in this simulation testing environment is meaningful for real world scenarios.

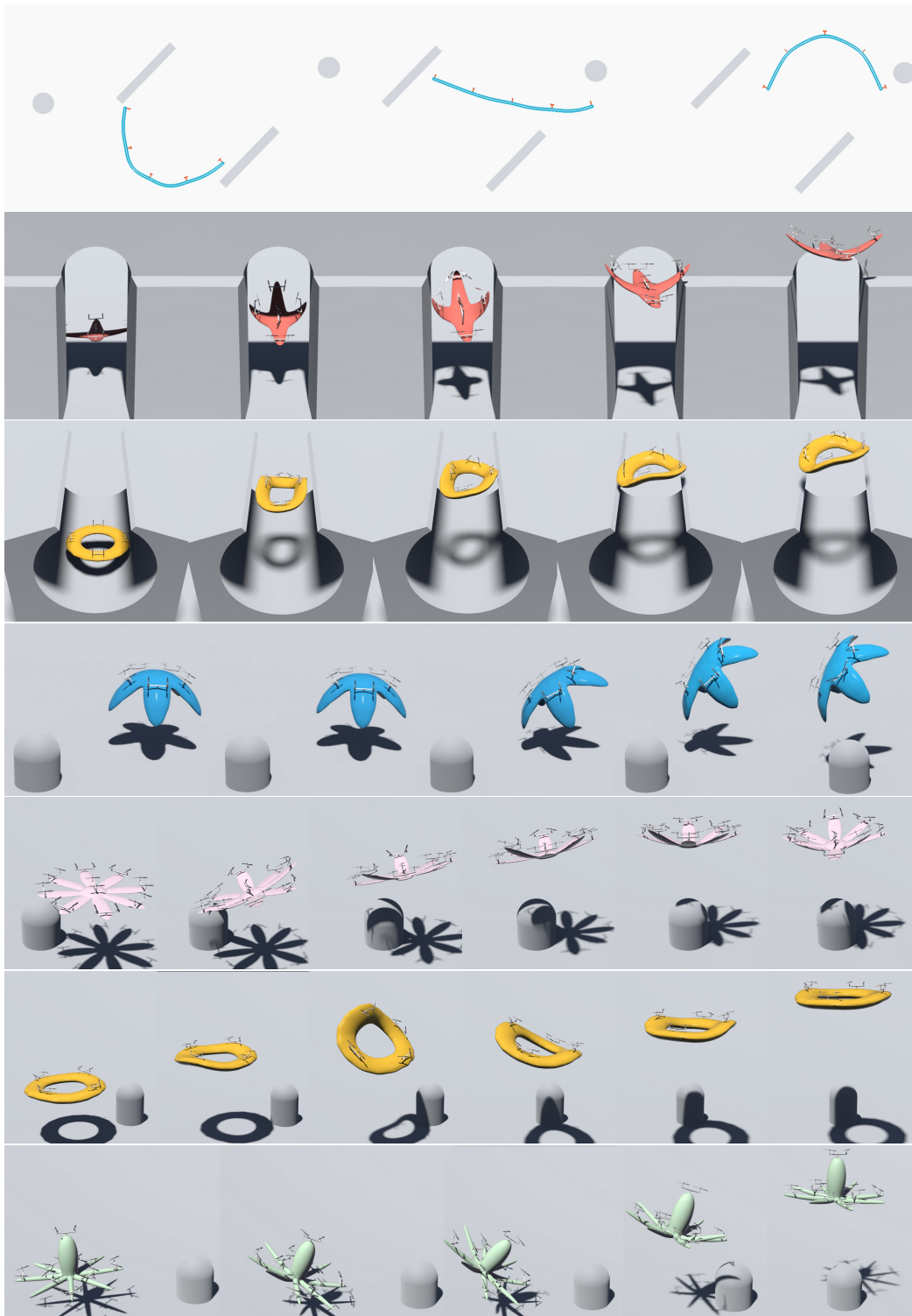


Figure 15: Visualization of more test results; Top 3: Obstacle avoidance animation; Bottom: Locomotion animation;